Important Notice

This copy may be used only for the purposes of research and private study, and any use of the copy for a purpose other than research or private study may require the authorization of the copyright owner of the work in question. Responsibility regarding questions of copyright that may arise in the use of this copy is assumed by the recipient.

UNIVERSITY OF CALGARY

Time-lapse rock physics inversion of thermal heavy oil production

by

Evan Peter Mutual

A THESIS

SUBMITTED TO THE FACULTY OF GRADUATE STUDIES

IN PARTIAL FULFILMENT OF THE REQUIREMENTS FOR THE

DEGREE OF MASTER OF SCIENCE

GRADUATE PROGRAM IN GEOLOGY AND GEOPHYSICS

CALGARY, ALBERTA

June, 2018

© Evan Peter Mutual 2018

Abstract

Time-lapse (4D) seismic monitoring of thermal heavy oil production represents a simple, robust and cost-effective method of characterizing changes in reservoir conditions. Conventional 4D seismic monitoring techniques track changes in a reservoir by comparing differences in seismic amplitudes and traveltimes over calendar time. These amplitude differences offer insight into the spatial extent of production and injection effects, but the physical cause of the observed amplitude differences is ambiguous. In order to properly distinguish between the effects of heated oil, steam, pressure, and temperature more information must be extracted from the seismic data. In this study, I combine AVO analysis and rock physics modeling in a rock physics inversion to quantify petrophysical changes in the reservoir thereby offering a more complete description of subsurface conditions during SAGD operations. With the resulting estimates for change in steam and heated oil saturations, the differentiation between varied fluid responses is possible. The heterogeneity of the SAGD operation is clearly observed. Areas surrounding the western well pairs with little to no steam or heated oil present contrast significantly with the large changes observed along the well pairs to the east. This leads to opportunities for improved production efficiency through the identification of zones with significant steam baffles and barriers, which significantly increase steam and energy requirement and prioritizing production of more efficient zones. Heated oil maps can also aid in identifying the most efficient zones and help track the mobilized bitumen to ensure it is not escaping or situated beyond the reach of the production wells. Together, results of this kind give operators valuable feedback that helps reduce both costs and environmental footprint for SAGD operations.

Acknowledgements

There are many people that I would like to thank for their help in finally completing this thesis. Some of these people have had a direct, tangible contribution to this study and others' impact may have come in a more indirect form. While many of these acknowledgments are predictable or cliché in nature, that should by no means diminish the fact that this work would not have been completed without the collective help of these people and probably many others that I'll forget to mention. To begin, I'd like to thank my supervisors Dr. David Cho and Dr. Kris Innanen, who in addition to helping with every part of this work also managed to bear with me and maintain a good humour as I needlessly and lazily dragged my feet in completing this thesis. Second, although they didn't provide any direct contribution and I probably went out of my way to de-emphasize the importance of their support or pretend it wasn't needed, I have to thank my mom Wanda Mutual and my sister Alycia Mutual who are always there to hear me variously complain, brag, feign apathy and whatever else it is that I did, do and will do. You guys are the best. Third, although he passed away before this work even began, I would be beyond remiss if I didn't offer a shout out to my dad Larry Mutual who helped make me who I am and taught me how to learn from mistakes, both my own and others'. Finally, as this is dragging on and has started to seem like I'm purposely adding fluff to prop up this work, I'll group the numerous others who have supported and shaped me into one final thank you. This list is undoubtedly incomplete, but includes the rest of my family, my amazing friends, other geophysics students in undergrad and at CREWES, my teachers, my professors and all the staff and various interconnected web-work that somehow lead to this relatively small achievement. Thanks.

Dedication

This thesis is dedicated to the late George Carlin, who poignantly expressed the value of humility and the mundanity of ego with the following quote about honour roll bumper stickers "Here's a bumper sticker I'd like to see: Proud parents of a child whose self-esteem is sufficient that he doesn't need us promoting his minor scholastic achievements on the back of our car."

Table of Contents

List of Tables

List of Figures and Illustrations

List of Symbols, Abbreviations and Nomenclature

Symbol	Definition
3C	Three component
4D	Time-lapse
AI	Acoustic impedance
AVO	Amplitude versus offset
CMP	Common midpoint
CSS	Cyclic steam stimulation
EOR	Enhanced oil recovery
NMO	Normal move-out
PSTM	Pre-stack time migrated
RMS	Root mean squared
SAGD	Steam-assisted gravity drainage
SI	Shear impedance
Vp	P-wave velocity
Vs	S-wave velocity
Vp/Vs	P-wave velocity divided by S-wave velocity

Chapter 1 – Introduction

1.1 – Oil sands overview

With an increasingly competitive worldwide energy market and low energy prices, the economic viability of any natural resource target is dependent upon our ability to harness said resource in a manner as efficient and safe as possible. In 2014, total Canadian oil production was 3.7 million bbl/d with oil sands production from Alberta accounting for 2.2 million bbl/d (Canadian Association of Petroleum Producers, 2015). Due to the highly viscous, biodegraded properties of bitumen, oil production of Alberta's oil sands requires strip mining, or enhanced oil recovery (EOR) methods for extraction, and yields less valuable products after refining. As such, oil sands projects require large up-front capital and are often only economically viable if certain production efficiency thresholds are met.

For in-situ production of bitumen, there is a large energy input requirement to reduce viscosity until bitumen will flow. Figure 1-1 compares the viscosity of various fluids and quasi-fluids with temperature. From this figure, one can see that bitumen requires a substantial increase in temperature from in-situ conditions in order to lower its viscosity to that of conventional oil. The energy cost for this temperature increase is high both economically and environmentally. Monitoring and optimization of oil sands operations is therefore essential to long-term project success. These projects have long life cycles, and even marginal gains in operational efficiency translate directly into cost savings through injection or steaming optimization, de-risking of in-fill well drilling and caprock integrity monitoring among others. In order to improve operational efficiencies, one must have a detailed understanding of reservoir conditions during steaming and production. Point data, such as monitoring wells or production data, can offer insight into reservoir conditions, but have high costs and little to no spatial coverage. Time-lapse (4D) seismic monitoring is a simple, relatively low cost, and robust method of remotely monitoring changes in reservoir conditions over entire development fields.

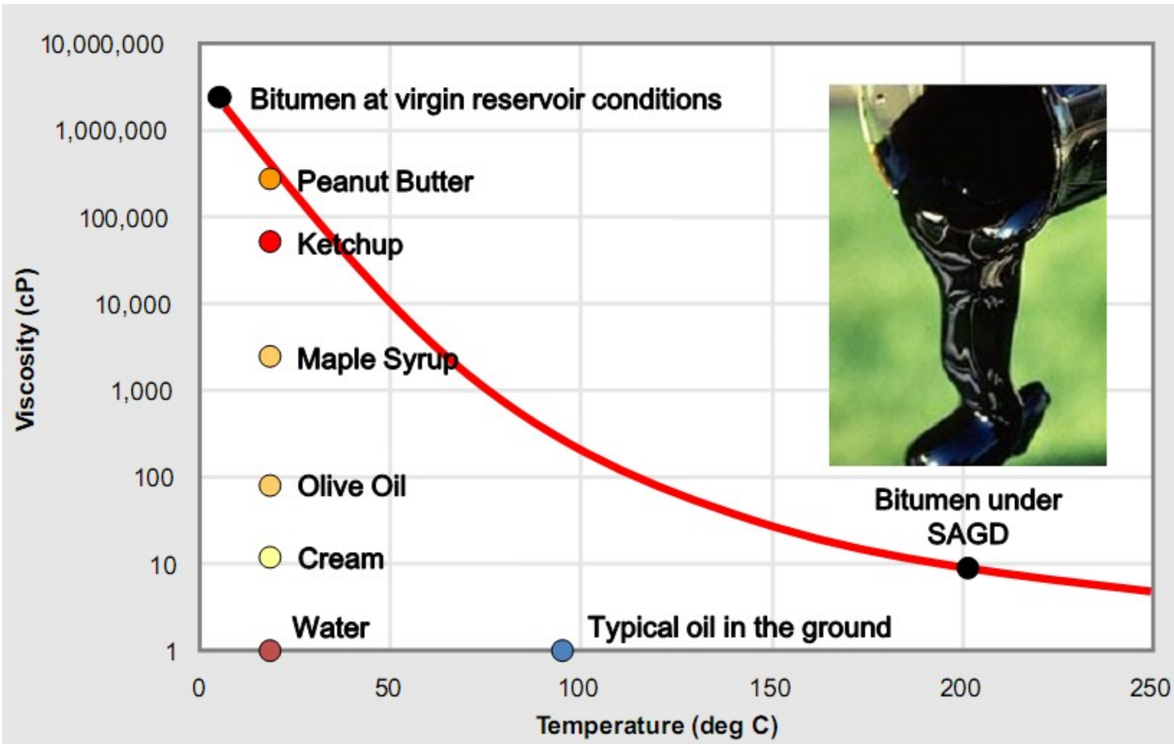

Figure 1-1: Bitumen viscosity progression with temperature compared to typical values (from ConocoPhilips, 2015).

1.2 – Geophysics overview

Geophysics is the study of the Earth, its properties and its processes using quantitative methods based on physical principles. Reflection seismology is a subset of geophysics that studies the propagation of elastic waves through the Earth. The basic principles of reflection seismology are closely aligned with echolocation in bats and medical ultrasound technology wherein reflected acoustic or elastic waves are used to create an image. Rock physics describes the quantitative link between elastic rock properties describing the rigidity and stiffness of a rock and petrophysical parameters describing the mineralogy, porosity and fluid composition of a rock. This study focuses on combining these two disciplines through rock physics inversion whereby reflection seismic data is processed and analyzed and combined with a rock physics model to estimate the petrophysical parameters of the subsurface.

Multiple sets seismic data acquired at different periods of time over the same area is referred to as time-lapse, or 4D seismic data. Each seismic dataset taken at a specific period of time is referred to as a seismic vintage. The first seismic vintage is often denoted as the baseline and subsequent vintages are denoted as monitors. 4D seismic interpretation involves studying varying seismic reflection response with time in order to infer and map changes taking place over time.

An inverse problem involves calculating a model from a set of observations. In reflection seismology, the observations refer to reflection seismic data and the model refers to a model of the subsurface that produces those reflections. In amplitude versus offset (AVO) inversion, the idea is to calculate the elastic model of the subsurface that produced the angle-dependent reflection amplitudes observed in seismic data. In this study, AVO inversion is extended into the time-lapse domain, whereby we calculate the changes in elastic properties of the subsurface that produced the changes in angle-dependent reflection amplitudes.

1.3 – Geophysics in oil sands

Bitumen reservoirs in Alberta offer unique geophysical challenges and opportunities. Because of high in-situ viscosity, these reservoirs must be produced using EOR methods such as cyclic steam stimulation (CSS) or steam flood methods such as steam-assisted gravity drainage (SAGD). These EOR techniques are associated with time-lapse responses that are easily observable in real seismic data. A simple schematic detailing SAGD is shown in Figure 1-2. Two well bores are drilled horizontally on top of one another. Steam is injected in the upper well-bore in order to reduce bitumen viscosity, allowing the heated oil to flow down to the lower well-bore where it is produced. The existence of technology to remotely monitor steam chamber growth, including potential baffles and barriers, in addition to identifying out-of-zone heated oil or gases, represents a significant opportunity to optimize production efficiency while limiting environmental footprint. The premise of 4D seismic interpretation is that all desirable and undesirable production related effects change the properties of the subsurface, which manifest as changes in the acquired seismic signature. 4D seismic interpretation analyzes these changes and seeks to infer the actual change in the subsurface that caused the observed response. In oil sands reservoirs, thermal heavy oil production is manifested as time-shifts and amplitude changes between surveys. Unfortunately, the combination of fluid changes and temperature and pressure increases creates an ambiguity when interpreting time-shifts and increases and decreases in seismic amplitudes. An inverse problem involves calculating a model from a set of observations. 4D AVO inversion allows us to extract valuable quantitative information from seismic data that is otherwise lost when only comparing amplitude differences. The changes in elastic properties that result from 4D AVO inversion can then be mapped from elastic space into petrophysical space using a calibrated rock physics model. In this study, two seismic vintages were inverted simultaneously for changes in steam saturation and heated oil saturation. The 4D rock physics inversion results are immediately interpretable quantities that are intuitive to understand across multiple disciplines, making them ideal for informing real-time production optimization decisions.

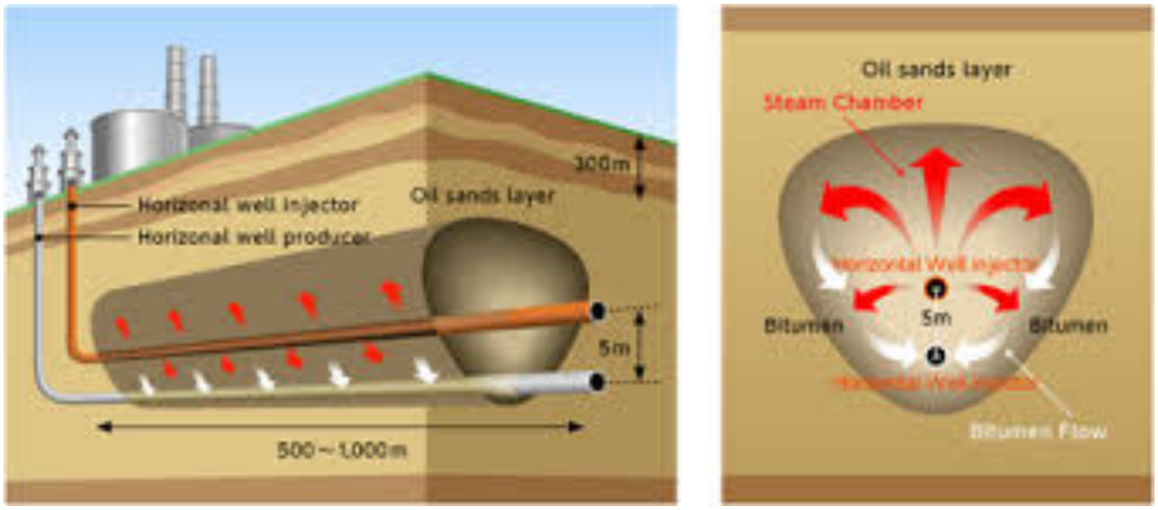

Figure 1-2: Schematic SAGD operation (from Japex).

1.4 – Survey information

The survey area for this project is located in the Athabasca Oil Sands region of Northeastern Alberta, Canada. The target of interest are the bitumen-saturated sands of the McMurray formation, a shallow, unconsolidated reservoir at a depth of approximately 300 meters below the surface. Both seismic data and geophysical well log data were used in this study.

4D processed pre-stack time migrated (PSTM) and normal moveout (NMO) corrected common mid-point (CMP) gathers and seismic stacking velocities were made available for the purposes of this study. From Yilmaz (2001), a CMP gather refers to the sorting of acquired seismic traces by common mid-point, where the mid-point is defined as the mid-point between shot and receiver locations. NMO describes how the travel times of seismic reflection events increase with increasing offset resulting in a parabolic reflection event shape. NMO correction flattens reflection events to the zero-offset travel time by applying time corrections calculated using the Dix equation (1955). Yilmaz (2001) describes seismic migration as the process by which dipping reflectors are moved to their true subsurface position and diffractions are collapsed to produce a true representative seismic image. The full processing flow also includes noise attenuation and ground roll suppression, surface consistent scaling, time-variant surface consistent deconvolution, statics analysis, spectral whitening and 5D trace interpolation and regularization. A detailed description of each processing step is not the subject of this study and is therefore not included, but descriptions of the various steps are found in Yilmaz (2001).

The baseline seismic survey was acquired in 2006 as an exploration survey using non-permanent geophone arrays. The monitoring survey (hereafter 'monitor') was acquired with permanent buried geophones in 2015, approximately 6 months after the start of steam injection. Due to the differences in acquisition, the baseline and monitors surveys had different initial geometries. As such, the surveys were cropped to the largest possible area covered by both dataset. The uncropped and cropped survey geometries are shown in Table 1.

Table 1: Survey geometries

	Baseline	**Monitor**	**Final**
In-line start	721	725	725
In-line end	873	871	871
In-line spacing (m)	10.00	10.00	10.00
Cross-line start	1235	1239	1239
Cross-line end	1356	1353	1353
Cross-line spacing (m)	10.00	10.00	10.00
Total number of traces	18666	16905	16905
Number of live traces	16918	15527	15426
Area (km2)	1.69	1.55	1.54

Both vintages were processed simultaneously in a 4D processing workflow to minimize any anomalous 4D changes caused by the acquisition differences. The 3D surveys were designed as higher resolution surveys with 10 x10 meter bin size, 1ms sample rate and 5D interpolation with nominal fold of over 100. They covered an area over a SAGD operation with a well pad containing 8 well pairs.

In addition to seismic data, three vertical wells located within the survey area were provided with full suites of both elastic and petrophysical well logs including caliper and gamma, compressional and shear sonic, density and volume of shale, total and effective porosity and water saturation logs. No production data were available at this time.

1.5 – Geologic setting

The Athabasca oil sands deposit is the largest of the three major bitumen deposits in Canada. The other two major oil sands deposits are Peace River and Cold Lake. The relative sizes and geographic locations of these deposits in Alberta are shown in Figure 1-4. The McMurray formation itself was formed in incised valleys during fluvial processes and transgressed marginal-marine environments, and is therefore generally characterized by high energy depositional sediments with coarse, fluvial deposits at the base and finer, lower energy marine sediments in the upper McMurray (Gingras and Rokosh, 2004). This assemblage unconformably overlies the Beaverhill Lake (BHL) group; a Devonian-aged interbedded carbonate and shale that is easily mapped seismically by a large impedance contrast (Kelly et al., 2015) between the hard, rigid Devonian rock and the overlying soft, unconsolidated sands of the McMurray formation. Comformably overlying the McMurray formation is the Clearwater formation consisting of interbedded sands and shales, which serve as an impermeable cap-rock to sequester injected steam during SAGD operations.

Figure 1-4: Regional extent of Athabasca, Peace River and Cold Lake oil sands deposits (from Hein et al., 2001)

1.6 – Previous time-lapse studies

Several important time-lapse studies of heavy oil reservoirs have been published over the last twenty years using various seismically derived attributes to map and differentiate changes in the subsurface. Jenkins et al. (1997) published a study over the Duri heavy oil field in Indonesia that related the time-shifts observed in seismic surveys shot at various intervals over 31 months. They were able to use the relatively dense temporal sampling of their study to observe subsurface velocity increases and decreases, which were then used in conjunction with 3D reservoir modeling to differentiate between increases and decreases in gas saturation and heated and cold liquid pore fluids. The authors' seismic observations correlated strongly with their reservoir modeling and demonstrated the utility of using time-shift data to remotely monitor steam-flooding operations. A limitation of this study is the single dimensional nature of the interpretation. The authors' reliance solely on time-shift measurements makes differentiating between multiple effects that slow wave propagation (e.g. increases in pressure, temperature and gas saturation) ambiguous. In their study, the ambiguity is resolved effectively using relatively high temporal sampling, but without this constraint, the method would suffer.

Kato et al. (2008) and Nakayama et al. (2008) published two accompanied papers on rock physics and 4D seismic surveys of the Hangingstone SAGD operation in Alberta, Canada. Kato et al. (2008) measured the changes in compressional (P) and shear (S) waves of a Hangingstone bitumen-saturated rock sample being subjected to a sequential process of changing first pressure, then temperature, and finally fluid fill, to replicate SAGD operations in a controlled laboratory setting. The authors derived empirical relationships relating P and S wave velocities for differing pressure and temperature conditions. By simplifying the SAGD process into a sequential process wherein only a single change is considered at a time, this study effectively de-couples the varied effects taking place during SAGD operations. Unfortunately, in doing so, it limits the real-world applicability to SAGD operations wherein these effects are taking place simultaneously. Nakayama et al.'s (2008) accompanied paper uses the rock physics model developed by Kato et al. (2008) and various seismic attributes to classify the seismic response of a 4D survey of the Hangingstone field. The authors used time-shifts, RMS amplitude and cross-correlations to classify the observed seismic anomalies into like categories. Unfortunately, the inclusion of non-physical seismic attributes such as RMS amplitude and cross-correlations makes this classification largely qualitative. It can, therefore, not be used to estimate actual elastic or petrophysical changes in the subsurface.

Following a similar approach, Kelly and Lawton (2013) used attribute analysis of time-lapse seismic data to delineate steam chamber development. In this study, baseline and monitor surveys were processed and subsequently, various attribute differences were extracted from the processed full-stack volumes to map reservoir changes. The authors used amplitude differences, time-shifts, frequency analysis and isochronal analysis as primary means to map changes in the reservoir due to production. Frequency analysis demonstrated a sharp decrease in high frequency content in the monitor survey below the interpreted steam chambers. This frequency attenuation was interpreted as caused by the additional presence of steam in the monitor survey that was initially absent. As described by White (1975), a compressional wave traveling through a rock causes pressure gradients in the pore fluid leading to fluid flow. In the case of multi-phase pore fluids, such as water and gas, these pressure gradients become quite large and cause significant amounts of fluid flow and thus significant energy losses in the wavefield manifesting as an observed attenuation. Using the various seismic attribute volumes, the authors mapped the spatial changes in the reservoir due to steaming and production. Unfortunately, a shortcoming of this approach is that the binary attribute analysis does not differentiate between steam, oil, pressure and temperature and does not offer an ability to quantify the changes in the reservoir in a physically meaningful way.

Multi-component (3C) 4D joint seismic inversion studies carried out by Gray et al. (2016) and Zhang and Larson (2016) demonstrated that using converted wave (PS) seismic data yields a 4D Vp/Vs low-frequency model that improves our ability to map heated oil. Performing 4D AVO inversions over thermal heavy oil reservoirs allowed the authors to estimate actual elastic property changes in the reservoir. By combining PP and PS time shift data, the authors created a 4D Vp/Vs low-frequency model that mitigated the band-limited response of the available seismic data to yield improved Vp/Vs inversion results. Subsequently, using Kato et al.'s (2008) rock physics model as a basis for interpretation, the authors were able to differentiate between a steam and heated oil response using either a decrease or an increase in Vp/Vs as a direct indicator. This work demonstrates the ability of 3C-4D AVO inversion to extract more information from our seismic data, but ultimately classifies changes into two discrete categories thus losing the ability to interpret relative spatial changes. Moreover, by using PS data as the primary means to identify heated oil, the workflow presented in these studies would be insufficient for interpretation with only PP data.

Studies by Przybysz-Jarnut et al. (2015) and Barker and Xue (2016) demonstrated that 4D seismic is an effecient tool for real-time production optimization; the researchers derived new rock properties from daily seismic surveys to track reservoir changes. These works follow similar logic to that of Jenkins et al. (1997). The authors derived relative acoustic impedance and relative change in velocity properties from time shift and RMS amplitude differences. Using very high temporal sampling involving daily seismic surveys, an instantaneous daily temporal derivative is calculated that provides a measurement of change in the reservoir on a daily basis. Within such a measurement scheme, a single production effect is more likely to dominate, allowing the interpreter to ignore the coupling with other subsurface changes.

Shopra et al. (2010), Gray et al. (2015) and Gray et al. (2018) discussed the importance of AVO inversion for density in bitumen-saturated reservoirs. Shopra et al. (2010) and Gray et al. (2015) found that in a 3D AVO inversions, better correlations were found between petrophysical quantities such as volume of shale and porosity and density than to acoustic impedance and

Vp/Vs. In particular, Gray et al. (2015) noted almost zero correlation between acoustic impedance and porosity, volume of shale and water saturation compared to upwards of 65% correlations between these quantities and density. This study also noted a markedly more accurate density inversion result than shear impedance inversion result and suggested that this could be due to the fact that as McMurray sands are under-pressured and unconsolidated, they behave as a slurry and have a very low effective shear modulus. As such, the AVO response is postulated as driven more by density than by shear properties. Importantly, these observations on the importance of density are less relevant in the time-lapse sense. As the densities of bitumen, heated heavy oil and water are extremely similar, we do not expect a time-lapse density response for a change from bitumen to heated oil or water. Gray et al. (2018) studied the time-lapse response of SAGD operations and examined the theoretical evolution of acoustic impedance, shear impedance, Vp/Vs ratio and density. Acoustic impedance and shear impedance would decrease throughout the SAGD process by varying slopes depending on the particular transition; Vp/Vs would either increase or decrease depending on the replacement of bitumen by heated oil or steam; and density would only show a response when either bitumen or a liquid phase is replaced directly by steam. As such, the authors chose to use an AI, Vp/Vs 4D inversion parameterization to interpret the time-lapse response. This observation helped inform the choice the inversion parameterization for this study.

1.7 – Thesis objectives

The primary objective of this study is to quantitatively characterize reservoir conditions during thermal heavy oil production using surface seismic data. As an extension to the studies mentioned in Section 1.6, this study will use calibrated rock physics modeling in conjunction with 4D AVO inversion to perform a 4D rock physics inversion that has the ability to directly quantify changes in petrophysical parameters such as steam or gas saturations, heated oil saturations and pore pressure changes using only PP seismic data. In so doing, we demonstrate the effectiveness of using remotely sensed geophysical methods to improve economic and environmental sustainability of thermal heavy oil projects.

Chapter 2 – Rock physics

2.1 – Overview of rock physics

Rock physics analysis is a critical first step in quantitative seismic interpretation. The analysis studies the relationship between petrophysical and/or geomechanical properties and elastic properties derived from seismic. The resulting rock physics model provides a crucial link between geology and/or engineering and geophysics. For a time-lapse study in oil sands reservoirs such as the McMurray formation, this means using elastic inversion results and a calibrated rock physics model to quantify in-situ porosity, volume of shale and bitumen saturation as well as time-lapse changes including gas saturation, heated oil saturation and pressure. In order to create a properly calibrated model suitable for thermal heavy oil reservoirs, one must consider the particular rock properties associated with poorly consolidated, bitumen-saturated rock.

Much work has been done in describing the response of increasing both heat and pressure in bitumen reservoirs. As shown previously in Figure 1-1, in order to lower the viscosity of bitumen, thereby mobilizing the bitumen, the reservoir temperature must be increased. The associated phase change from quasi-solid to fluid has a distinct character that can be captured in a rock physics model. Simultaneously, the injection of steam into the system causes a pressure increase that “pushes” the mobilized oil down towards the production well, which leads to a strong P-wave velocity decrease from the presence of gas in the system on the order of 30% (Batzle et al., 2004). Kato et al. (2008) illustrates this process experimentally in a step-by-step manner considering first pressure, then temperature and finally, fluid substitution. By measuring P and S wave velocities while making incremental changes to pressure, temperature and fluid saturations, Kato was able to derive experimental relationships relating Vp and Vs for different pressure and temperature conditions. The results of the experiment are shown in Figure 2-1.

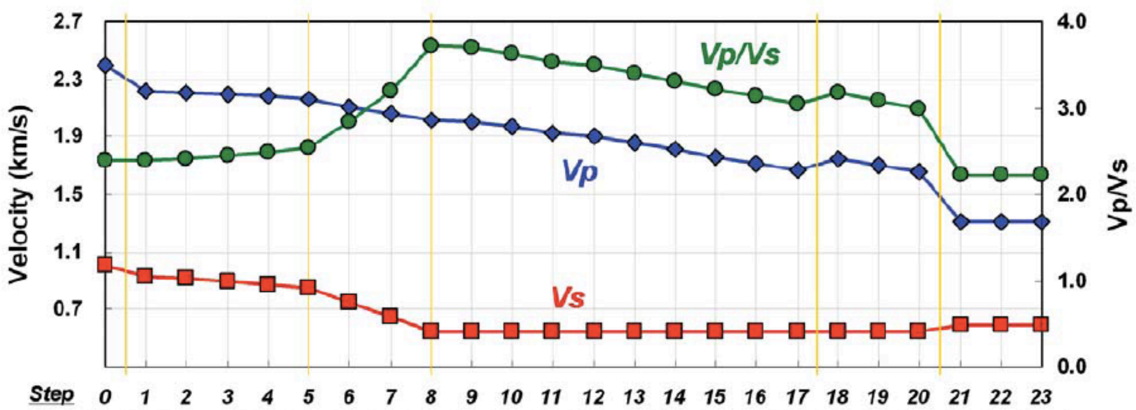

Step	0	1	2	3	4	5	6	7	8	9	10	11	12	13	14	15	16	17	18	19	20	21	22	23
Pp (psi)	300	300	400	500	600	700	700	700	700	700	700	700	700	700	700	700	700	700	700	700	700	700	700	700
T (°C)	10	10	10	10	10	10	15	20	25	30	50	70	80	100	120	140	160	180	200	220	240	260	280	300
Sw (%)	20	20	20	20	20	20	20	20	20	20	20	20	20	20	20	20	20	20	80	80	80	80	80	80

Figure 2-1: Sequential P and S wave and Vp/Vs ratio changes induced by steam injection (from Kato et al., 2008).

The most dramatic observable effect, and one that is characteristic of oil sands reservoirs, is during the heating process. As the bitumen is subject to heat, its shear modulus rapidly decreases to zero, resulting in a rapid decrease in shear wave velocity. When coupled with a relatively gradual decrease in compressional wave velocity, this rapid S-wave velocity decrease results in a dramatic increase in the overall rock frame's effective Vp/Vs ratio. This increase in Vp/Vs, coupled with a decrease in AI, is the signature of heated, movable oil in the reservoir. In contrast, areas surrounding the injection wells, where steam has been added to the system, a sharp decrease in the P-wave velocity coupled with minimal impact on the S-wave velocity should yield a sharp decrease in both AI and Vp/Vs ratio. For the purposes of this study, the 4D rock physics model will differentiate between these two characteristic responses, while acknowledging that directly coupled with and observed fluid changes are pressure and temperature changes that are sources of model uncertainty.

2.2 – Unconsolidated rock physics modeling

First, I will consider the poorly consolidated nature of shallow heavy oil reservoirs. Avseth et al. (2005), Bachrach and Avseth (2008) and Milovac (2009), among others, have shown that in such reservoirs, much higher Vp/Vs ratios are observed than those predicted by typical Greenberg-Castagna (1992) relationships. This is related to the assumption of non-slip (i.e. consolidated) contacts between grains associated with Greenberg-Castagna shear estimation methods. As a result, the observed shear modulus in poorly consolidated reservoirs tends to be lower than predicted yielding a characteristically high Vp/Vs ratio. This phenomenon is observed in the Vs vs. Vp crossplots shown in Figure 2-2. Here, cross-plots of Vs vs. Vp for 2 wells are shown colour coded by various petro-physical parameters. Also plotted are theoretical Greenberg-Castagna (1992) trend lines for sand, shale and mudrock in red, green and black, respectively. As the McMurray formation is a two mineral sand/shale reservoir with a dominant sand mineralogy, one would expect that the data would generally fall within the bounds of the sand (red) and shale (green) theoretical lines with a higher density distribution falling along the sand (red) line. Unfortunately, the measured well log data deviates significantly from this predicted behavior. If one were to use the standard published value of 44GPa for the shear modulus of quartz grains to constrain the rock physics model, the shear moduli of the other mineral end members in the multi-mineral regression would tend to be under-estimated. To account for this phenomenon in the model, I apply the workflow proposed by Bachrach and Avseth (2008) to regress the fractional volume of non-slip contacts in the reservoir to yield an optimized effective sand mineral end-member.

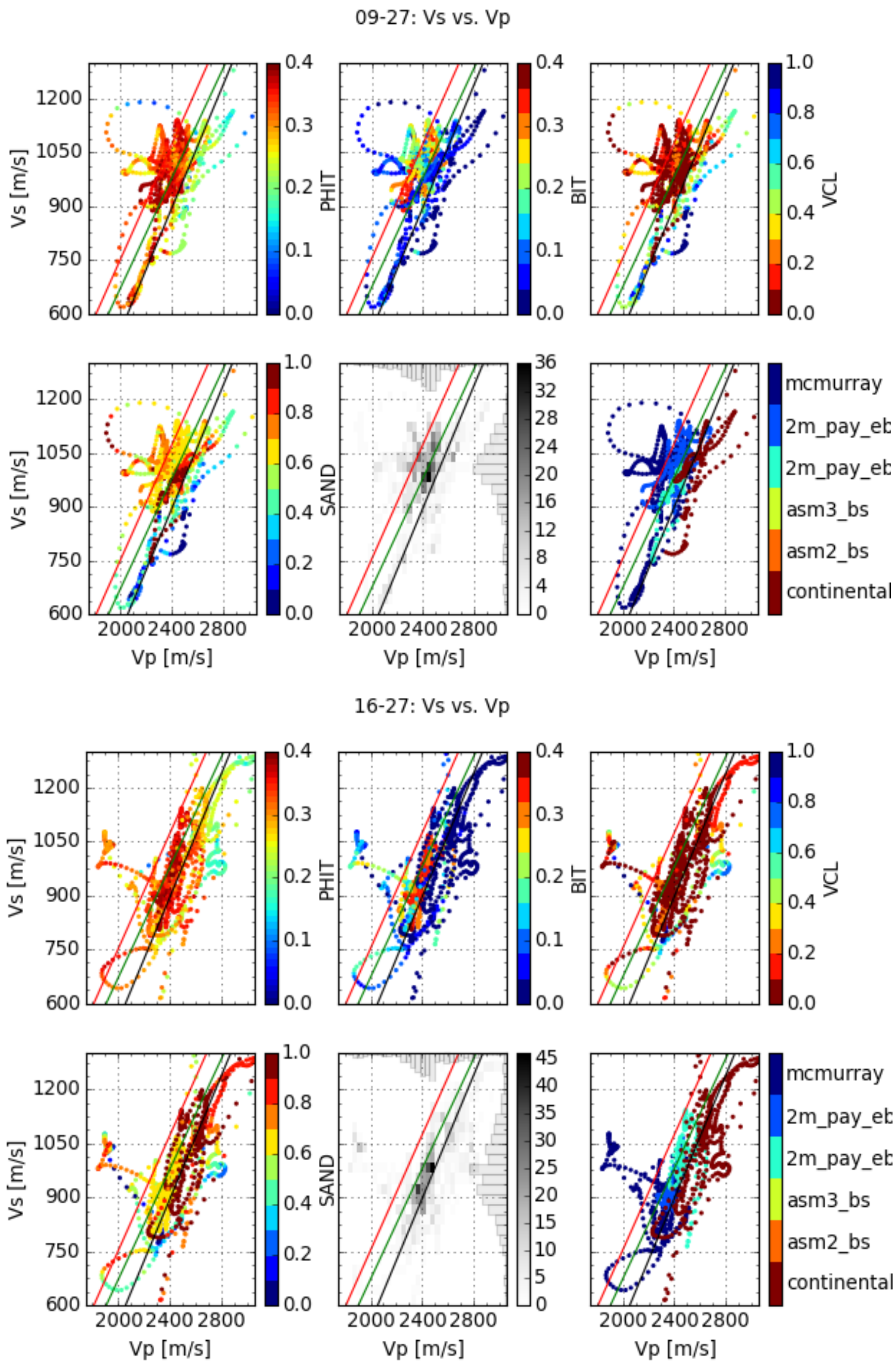

Figure 2-2: Vs vs. Vp cross-plots for two wells colour coded by petrophysical parameters and geologic tops.

In the following section, I provide a short review on the theory and workflow of Bachrach and Avseth (2008). Consider the normal and tangential stiffnesses given by

$$S_n = \frac{\partial F_n}{\partial \delta}, \quad S_t = \frac{\partial F_t}{\partial \tau}, \tag{1}$$

where F_n and F_t are the normal and tangential components of the force acting on a grain contact, and δ and τ are the normal and tangential displacement resulting from the applied force. If we then consider the grain matrix to be adequately modeled as two elastic spheres, we can describe the normal stiffness using the Hertz-Mindlin (1949) contact model, defined as

$$S_n = \frac{4aG}{1-\nu}, \tag{2}$$

where G is the mineral's shear modulus, ν is the mineral's Poisson's ratio and a is the contact radius between two spheres. then consider the tangential stiffness defined in the Mindlin (1949) model given by

$$S_t = \frac{8aG}{2-\nu}, \tag{3}$$

Finally, I define the effective bulk and shear mineral moduli described by Walton (1987) for a dry, dense, random pack of identical elastic spheres given by

$$K_{eff} = \frac{n(1-\varphi)}{12\pi R} S_n, \quad G_{eff} = \frac{n(1-\varphi)}{20\pi R}(S_n + 1.5 f_t S_t), \qquad (4), (5)$$

where φ is porosity, R is the grain radius, n is the coordination number and f_t is the volume fraction of non-slip contacts. We can then re-write the effective Poisson's ratio in terms of f_t yielding the following expression

$$\nu_{eff} = \frac{S_n - f_t S_t}{4S_n + f_t S_t} = \frac{2-\nu}{4(2-\nu)+2f_t(1-\nu)} - \frac{2f_t(1-\nu)}{4(2-\nu)+2f_t(1-\nu)}. \tag{6}$$

This equation is used to regress an estimate for the fraction of non-slip contacts in the reservoir. By taking the lower bound, where we assume zero tangential stress (or fraction of non-slip contacts equal to zero), we obtain the following expression

$$\nu_{eff} = \frac{S_n}{4S_n} = 0.25, \qquad \mu_{uncon\ sand} = \frac{3K_{sand}(1-2\nu_{eff})}{2(1+\nu_{eff})} = 22.2\text{GPa}, \tag{7}$$

which yields the lower bound of the sand shear modulus corresponding to a completely unconsolidated rock. The upper bound of the shear modulus is the standard theoretical quartz grain modulus of 44GPa. Subsequently, the lower and upper bounds are combined with the calculated value for f_t to obtain an effective sand mineral end member estimate that is more representative of the in-situ conditions. These equations do not account for any fluid saturations or mineral mixing and are therefore only valid in the dry, single mineral case. Consequently, in this study, the regression was performed using only data with volumetric clay less than 20% and water saturations greater than 70% to constrain the estimation to the most well behaved set of points. The resulting fraction of non-slip contacts was 0.37.

To demonstrate the results of Bachrach's workflow on this dataset, synthetic shear logs were generated using theoretical Greenberg-Castagna relations and using the newly derived unconsolidated relationships. The results for three wells are shown in Figure 2-3 with the associated statistics before and after correction in Table 2.

Table 2: Observed vs. modeled shear velocity before and after correction

Well	Greenberg-Castagna RMS Error	RMS Error after correction	Greenberg-Castagna correlation	Correlation after correction
1	15.00	5.00	0.70	0.85
2	9.74	6.24	0.49	0.58
3	11.04	5.36	0.53	0.84
Average	11.93	5.53	0.57	0.76

With the exception of the shale-rich continental formation, the misfit between the observed and modeled shear velocities has decreased. In particular, the average overall correlation between observed and modeled shear velocity has increased from 0.57 before correction to 0.76 after correction. The percent error has also decreased from 11.93 to 5.53. Part of the remaining misfit is due to the finite shear modulus associated with the bitumen that has not been yet been accounted for. It is also possible that the quasi-solid behaviour of the in-situ bitumen in some areas can act as cement for the grain matrix thereby increasing the similarity of the response to that of a typical, consolidated lithic rock. A fully calibrated model would ideally have a third mineral class of unconsolidated sand for each data point in the reservoir. Unfortunately, the theory for unconsolidated multi-mineral mixing in the presence of shale is not well developed, and changing this is beyond the scope of this study. Using the new effective sand mineral end-member bulk and shear moduli as a-priori model constraints, I now perform a multi-mineral regression analysis to obtain the elastic moduli of the remaining mineral constituents.

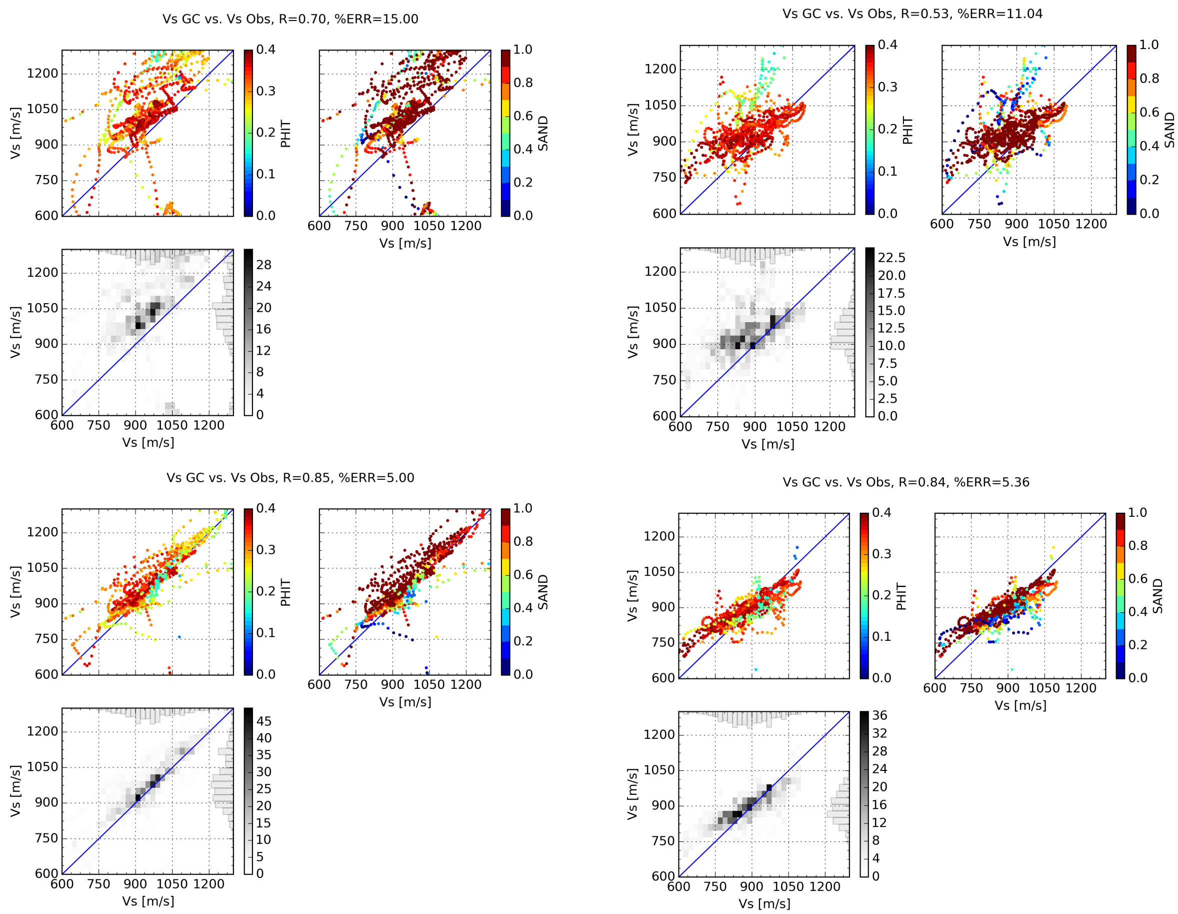

Figure 2-3: Modeled vs. observed shear logs for two well before (top) and after (bottom) applying correction for non-slip contacts.

2.3 – Petro-physical log re-normalization

The rock physics model used for this study is a non-linear regression based model (Westeng et al., 2009) that obeys physical bound theory and honors single and multi-mineral fluid substitution theory. The rock physics model is given by

$$\frac{1}{M+M_0} = \sum_i (1-\varphi)\frac{v_i}{M_i+M_0} + \frac{\varphi}{M_{fluid}+M_0}, \quad (8)$$

where M is an elastic (bulk or shear) modulus, φ is porosity, v_i is the volumetric fraction of the ith mineral, M_i is the elastic (bulk or shear) modulus of the ith mineral, M_{fluid} is the elastic modulus of the fluid and M_0 is a regression parameter that allows local trends of the field affecting the moduli such as pressure, temperature, cementation or matrix composition to be captured.

It is well established that bitumen behaves as a quasi-solid at in-situ conditions due to its high viscosity. As such, the elastic properties of the bitumen are not properly modeled by Batzle-Wang (1992) equations and typical Gassmann (1951) fluid substitution relationships do not apply. For the rock physics model, this means that bitumen has a finite shear modulus and should be considered as a third mineral in the rock physics modeling. To do this, I normalized the petrophysical logs a second time, to a three mineral model composed of quartz, clay and bitumen with remaining porosity being 100% water saturated. Figure 2-4 shows well tracks with various elastic and petrophysical properties before and after the re-normalization.

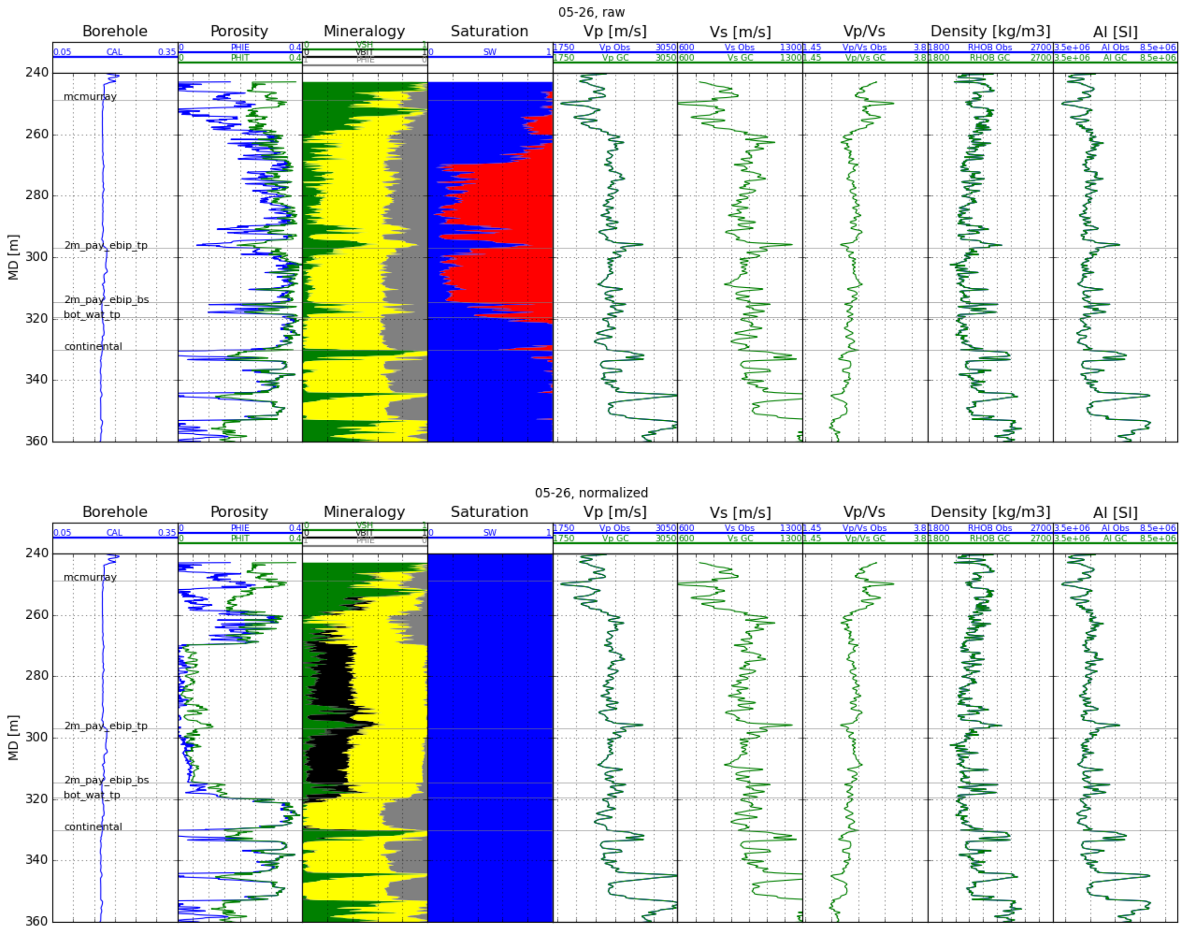

Figure 2-4: Well track showing petro-physics before (top) and after (bottom) re-normalization.

These re-normalized petrophysical logs are those used in conjunction with the elastic logs to estimate the in-situ rock physics model using equation 8.

2.4 – 3D rock physics modeling

Using equation 8 and the re-normalized petrophysical logs, a non-linear regression was performed to estimate the bulk and shear modulus for each mineral in the rock frame. By varying the regression parameter with different petrophysical parameters, we can optimize the model choice. The fit of the resulting rock physics models is tested by re-calculating the elastic logs using the petrophysical logs and the rock physics model and comparing the results with the observed values. For the purposes of this project, four regression parameters were tested including no regression parameter, porosity, volume of shale and volume of bitumen. The resulting estimated mineral moduli and associated percent errors are shown in Table 3.

Table 3: Elastic moduli and RMS error with varying regression parameters

Regression Parameter	Bulk Modulus Shale (GPa)	Bulk Modulus Bitumen (GPa)	% Error Bulk Modulus	Correlation Bulk Modulus	Shear Modulus Shale (GPa)	Shear Modulus Bitumen (GPa)	% Error Shear Modulus	Correlation Shear Modulus
None	41.5	3.9	13.64	0.59	3.8	0.1	21.96	0.54
Porosity	31.1	4.2	9.85	0.78	3.7	0.2	18.87	0.71
Volume of shale	26.2	4.5	13.61	0.59	2.1	0.4	22.03	0.54
Volume of bitumen	21.8	4.5	7.98	0.83	2.7	0.4	17.94	0.71

From these results, the model using volume of bitumen as a regression parameter has the lowest percent error for both bulk and shear modulus and was therefore considered to be the optimum model choice for this reservoir. Figure 2-5 compares the modeled and observed bulk and shear moduli colour coded by porosity, volume of bitumen, volume of clay, volume of sand, data density and geologic top for the chosen model. As seen most clearly in the data density plots, the majority of the data is falling roughly along the 1:1 line for both bulk and shear modulus, indicating the model is correctly capturing the rock physics trends of the reservoir.

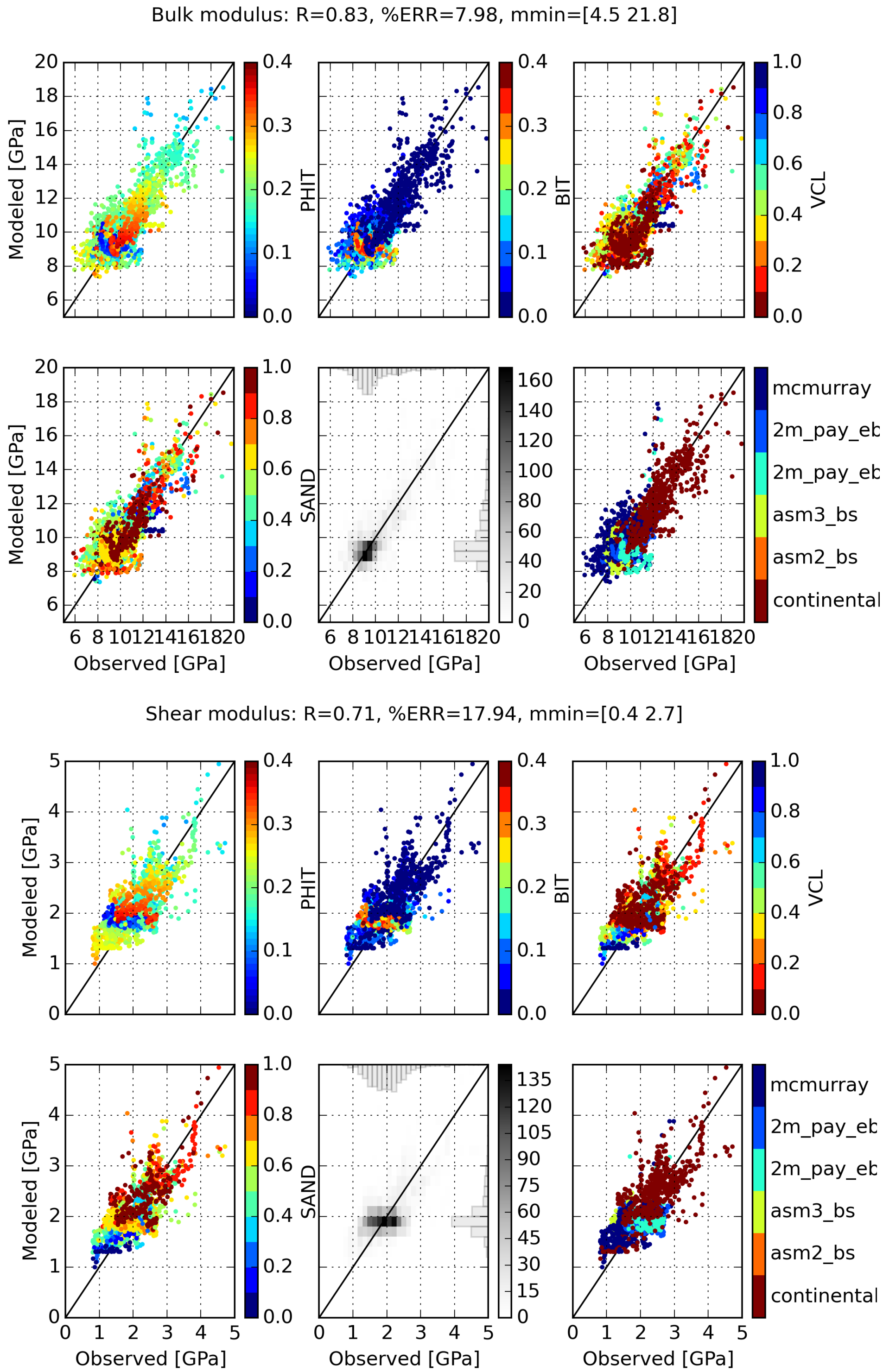

Figure 2-5: Modeled vs. observed bulk (top) and shear (bottom) modulus for optimum rock physics model.

Figure 2-6 shows the model fit in Vp/Vs vs. AI space, which is the inversion parameterization chosen for the project. Notice that in the modeled results we are not able to fully capture the scatter observed in the measured data, but the data density plots and associated histograms demonstrate that the majority of the modeled data are occupying the same area in elastic space as the measured data. The scatter in the measured data is attributed to well log errors associated with borehole quality or sonic log interpretation or slight deviations in fluid or mineralogical properties between wells that were not considered in the petrophysical model applied to the dataset.

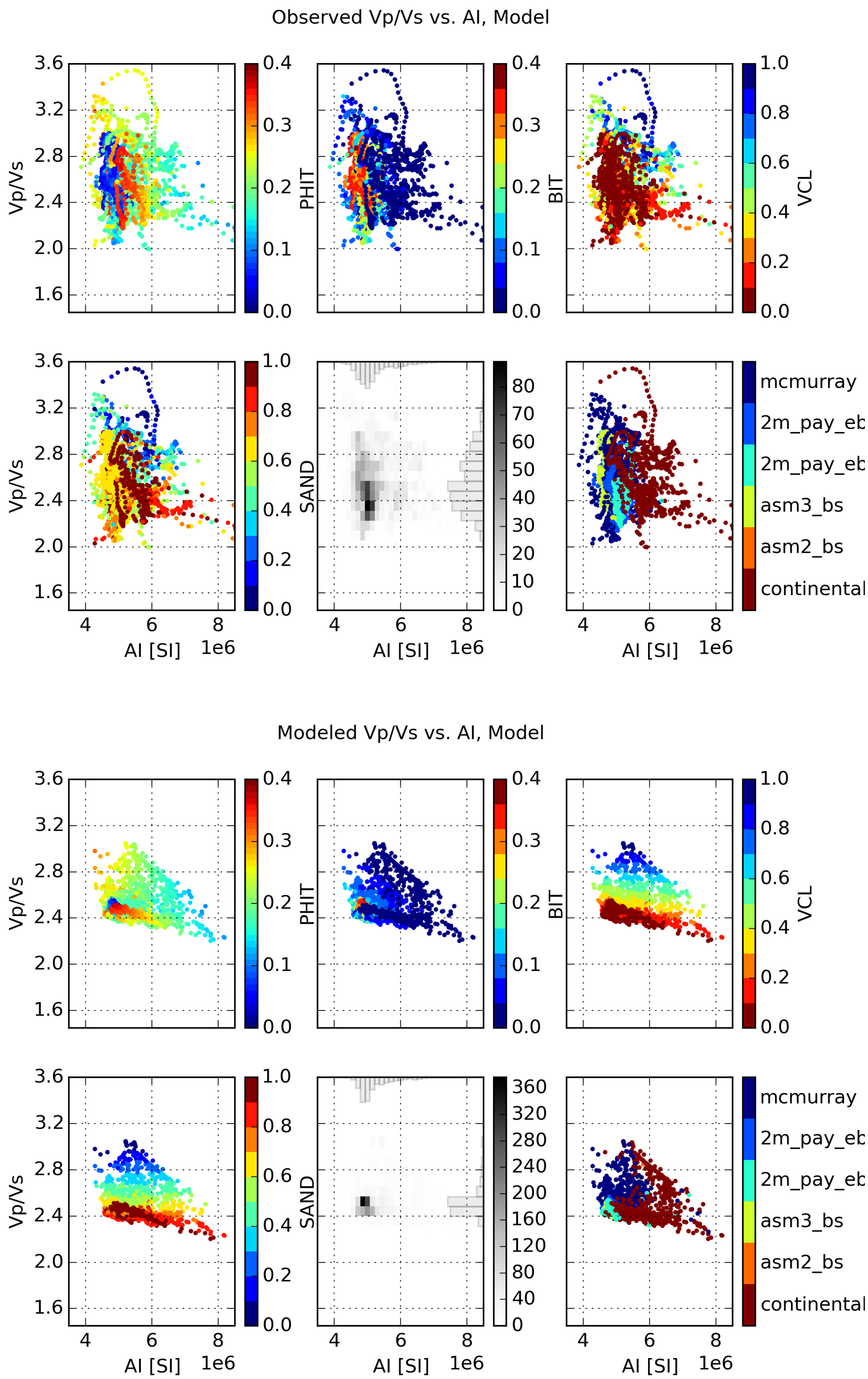

Figure 2-6: Observed (top) and modelled (bottom) data in Vp/Vs vs. AI space.

2.5 – 4D rock physics modeling

To investigate the rock physics response due to changes in pressure, temperature and fluid saturations, I made use of experimentally derived relationships based on the work done by Kato et al. (2008) to obtain a 4D rock physics model that can differentiate between bitumen, heated oil, water and steam. In an ideal circumstance, we would have several sets of measurements of the elastic properties for different phases of production, yielding a field calibrated time-lapse model, but in this case these calibration points were not available. In the absence of monitor logged or calibrated laboratory measurements, we will refer to Kato's (2008) study for the time-lapse rock physics model building. This model will serve as the basis for interpretation of the 4D AVO inversion results.

If 4D fluid calibration data were available, it could be easily incorporated into my 4D model using in-situ sand and shale mineral end-members (which would be assumed to be unchanged by pressure and temperature conditions), and substituting all the bitumen in the well log data with heated oil, steam or gas parameters. Unfortunately, lab data for the oil with changes in pressure and temperature were not available. As such, for the purposes of this study we will make use of the experimental relationships derived by Kato.

Several assumptions are made in this model derivation that differ from those in Kato's experiment. First, consider that Kato's experiment is performed in a step-wise manner. This method illustrates the unique responses of pressure, temperature and fluid changes, but in a real-world SAGD setting, many of these changes would be observed simultaneously. In particular, in Kato's experiment the steam addition is modeled in the last step as water is replaced by steam. In a SAGD operation, steam is injected into the reservoir at steam saturation conditions implying that steam exists simultaneously with pressure increases around the borehole. De-coupling these effects is beyond the scope of this study, but we recognize that the dominant response most likely to be observed in the 4D seismic at the wellbore will be the addition of a steam phase to the rock frame. For this 4D rock physics model, we will model the steam replacing bitumen in the reservoir.

To approximate the 4D response of the phase change of bitumen to heated oil we will use Kato's equations:

$$V_{p_{oil}} = (-0.0043T + 1.04)V_{p_{obs}}, \tag{9}$$

$$V_{s_{steam}} = (-0.0239T + 1.24)V_{s_{obs}}, \tag{10}$$

where V_{oil} is the velocity (acoustic or shear) of the rock in km/s, T is temperature in degrees Celsius and V_{obs} is the observed velocity (acoustic or shear) from well logs. In this case, as we are not trying to track the progression of the velocity, but obtain a value for the end member of pure heated oil, we let the shear modulus of the fluid equal zero and use equation 9 with a temperature of 25 degrees Celsius to estimate the change in acoustic velocity. Figure 2-7 shows the 4D rock physics model in Vp/Vs vs AI space.

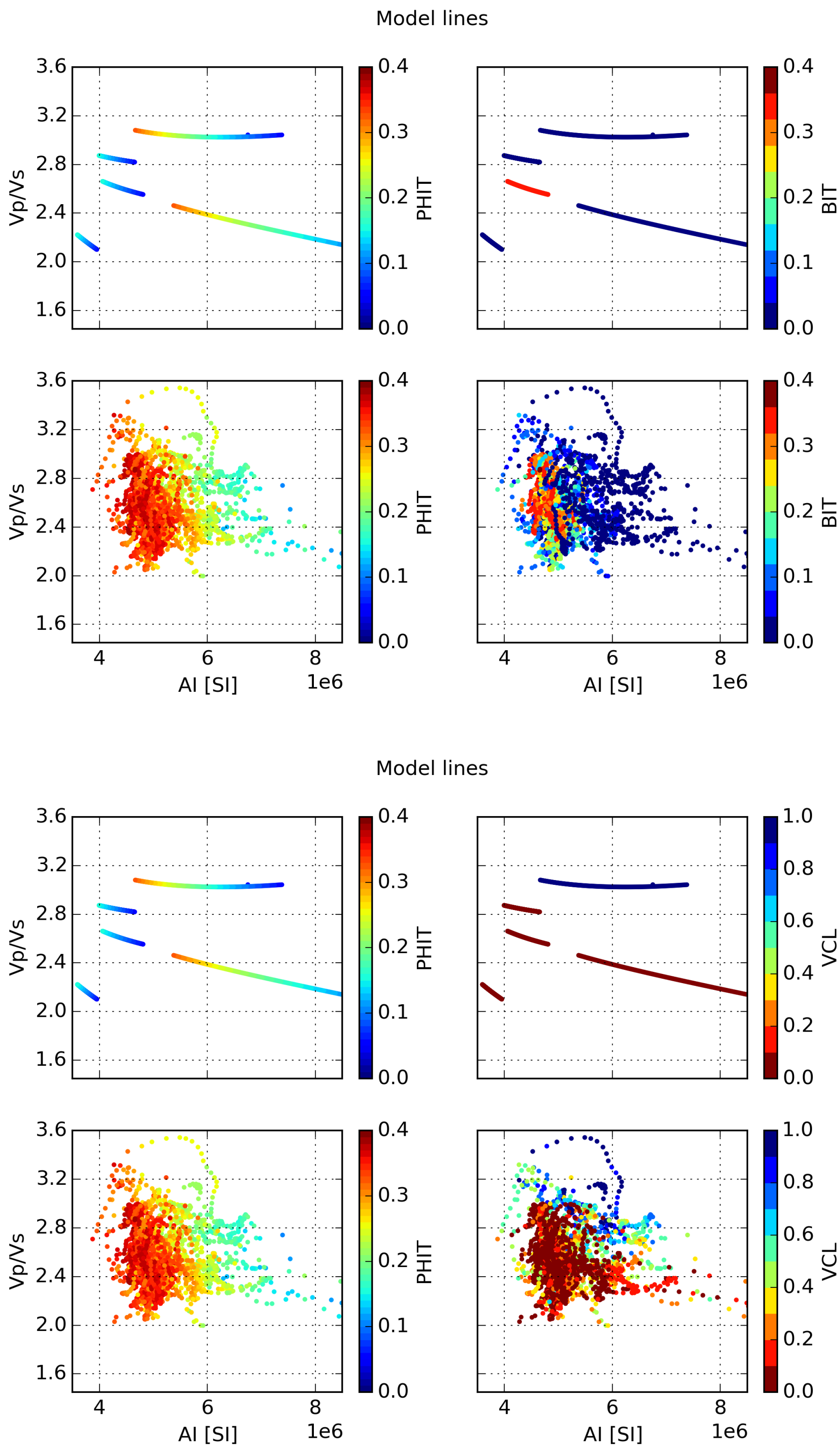

Figure 2-7: 4D rock physics model with porosity trend lines for brine sand, brine shale, steam sand, bitumen sand and oil sand colour coded by porosity and volume of bitumen (top) and porosity and volume of clay (bottom).

2-5 – Limitations and data quality issues

As with any modeling exercise, a proper assessment of the experiment's success should contain an analysis of data limitations. In this case there are several uncertainties that can be addressed. First, the 4D rock physics model that was created is an oversimplification of the actual effects being observed in the subsurface. Because of the lack of calibration data, in this study the classification of 4D effects is limited to fluid changes, but, we know that coupled with and fluid changes are temperature and pressure influences that are not being accounted for, which will therefore limit the overall accuracy of the rock physics inversion results. Additionally, secondary effects resulting from the fluid, temperature and pressure changes such as compaction, dilatation, thermal expansion, chemical changes and others could be causing time-lapse responses, and these are not considered in this study. All of these secondary effects can also impact production decisions. Fluid saturation changes were the focus of this study as they most directly showcase the ability of time-lapse seismic to provide results that can be used to quickly identify obvious production deficiencies. These deficiencies may include sub-optimal steam chamber development caused by baffles and barriers, escaped steam or gas and residual or escaped heated oil leading to infill well drilling opportunities.

In addition to rock physics modeling, access to a full suite of both petrophysical and elastic logs allows for an improved ability to identify any data quality issues that may be present in the logs. This step is extremely important to any successful AVO inversion workflow as elastic well logs are used as inputs to wavelet estimation, low frequency modeling and as inversion result calibration and validation. It is important that any data quality issues are identified prior to these steps in order to ensure results are not biased to bad quality data. As a by-product of rock physics modeling, we can examine how the elastic logs coincide with the petrophysical logs. If coherent trends are observed that roughly follow theoretical expectations, such as Greenberg-Castagna trends relating compressional and shear sonic logs or the Gardner (1974) equation relating compressional sonic and density, we can be confident that those data have a higher likelihood to be of good quality. In poorly consolidated reservoirs such as the McMurray formation, there is a higher occurrence of poor borehole conditions, which tends to negatively impact log measurements. Density logs are particularly susceptible to inaccuracies due to poor borehole conditions. Typical long range detectors of density tools have approximately 80% of its signal from within 10cm of the borehole wall, which is the shallowest investigation depth of all standard well logs (Rider and Kennedy, 2011). Any density log errors will cause errors in any AI calculations. Additionally, we see from Figure 2-2 that there are many data intervals with "stringers" in Vs vs. Vp space that appear unrealistic. In practice, shear velocities contain a higher degree of uncertainty as the shear wave arrival is embedded in a mix of arrivals within the sonic logging tool (Lines et al. 2010). These inaccuracies potentially lead to large discrepancies in the Vp/Vs ratio. As will be discussed in greater detail in Chapter 4-3, the shear log is an input to angle-dependent wavelet estimation. As such, inaccurate shear logs will negatively impact wavelet estimation. To suppress this bias, intervals with obvious log issues were edited with the shear logs predicted by the rock physics model. The edits were made if the observed shear wave velocity differed from the predicted values by greater than 30%.

Chapter 3 – Seismic pre-conditioning

3.1 – Seismic angle stack generation

As inputs to the 4D (i.e., time lapse) amplitude-variation-with-offset, or AVO, inversion, seismic angle stacks from derived from pre-stack time migration and NMO-corrected CMP gathers must be generated. The goal is to obtain data which can be interpreted in terms of the reflection strength equations due to Zoeppritz and/or Aki and Richards (Aki and Richards, 2002), but which have low noise and sufficient fold. For this study, angle computations were performed using Walden's (1991) 4th order angle approximation, using as input the RMS and interval velocity fields supplied by the processors of the data. Figure 3-1 shows an angle decomposition plot with seismic traces overlain by computed angle ranges, the resulting angle stack response and the filtered input velocity fields. Using angle decomposition plots as a guide, eight angle stacks were chosen with ranges from zero to fifty degrees as follows: $0^{\circ} - 13^{\circ}$, $13^{\circ} - 20^{\circ}$, $20^{\circ} - 26^{\circ}$, $26^{\circ} - 31^{\circ}$, $31^{\circ} - 36$, $36^{\circ} - 41^{\circ}$ and $41 - 45^{\circ}$. As shown in Figure 3-1, these angle ranges result in relatively uniform fold distribution through the reservoir zone and strike a balance between data quality and AVO response sampling.

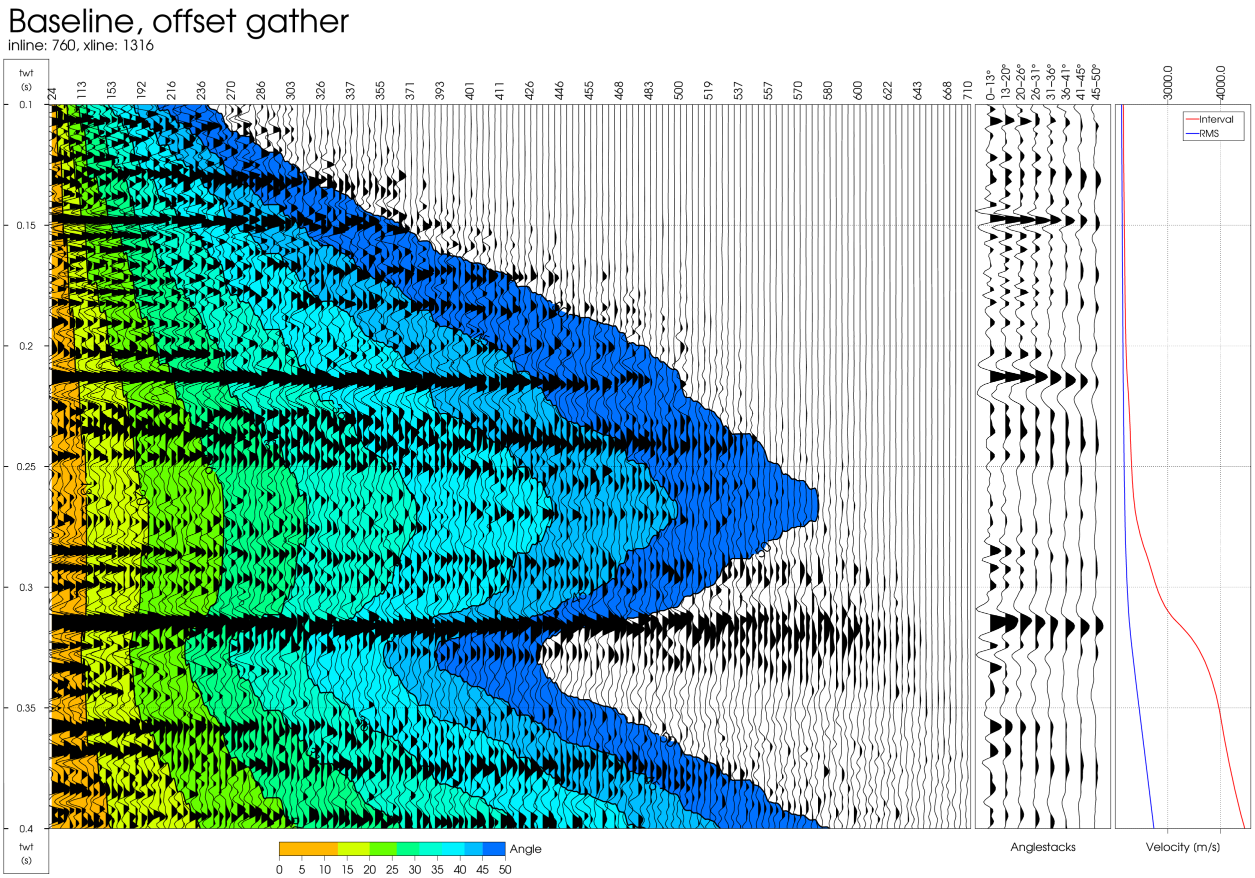

Figure 3-1: Angle decomposition plot of a baseline CMP gather (note: traces have been decimated by factor of two).

3.2 – 4D seismic data pre-conditioning

To ensure accurate and consistent results in the 4D AVO inversion, it is necessary to apply a preconditioning workflow designed to reduce noise and match the data between vintages while preserving the 4D changes related to steam injection and production. Without this essential step, 4D anomalies due to differences in acquisition, processing and travel times are incorrectly identified as physical changes in the subsurface. Depending on the level of repeatability between vintages, an optimized pre-conditioning workflow must be tailored specifically to the project. In this case, the pre-conditioning steps included, 1) low-pass filtering to eliminate high frequency noise outside the bandwidth of the 4D anomalies, 2) exponential gain correction to account for time related differences in amplitude levels, 3) spectral matching to stabilize the wavelet across the two vintages and 4) 3D seismic warping to account for travel time and/or imaging differences as a result of velocity changes in the reservoir due to steam injection.

3.2.1 – Low-pass filtering

A simple low-pass filter was used to cut out frequencies higher than 200Hz. Initial testing revealed that data in frequencies higher than this range were predominantly noise and outside the bandwidth of the expected 4D anomalies. The very marginal uplift in resolution observed when including frequencies above 200Hz was outweighed by the addition of significant high frequency noise.

3.2.2 – Exponential gain correction

In spite of the 4D consistent processing applied to the two datasets, there were noticeable differences in the gain correction applied to each vintage. To correct for this, RMS amplitudes in zones above and below the reservoir interval, where little to no change was expected, were compared between the two surveys. In particular, the monitor survey had too low amplitudes above the reservoir and too high amplitudes below the reservoir. An exponential gain correction was applied to the monitor to more closely match the baseline. The process was to calculate RMS amplitude levels above and below the reservoir and compute a difference in decibel drop between the two surveys. A smoothly varying time-variant scalar correction was then derived and applied to each sample with the following formula

$$A_{new}(t) = A_0(t) * e^{(t+1)p}, \tag{10}$$

where A_{new} is the new amplitude, $A_0$is the original amplitude and $p = \log 10^{\frac{ref_{dbdrop} - in_{dbdrop}}{20}}$. In order to preserve the true 4D anomalies in the reservoir, the time-variant operator was designed to have scalar values of 1 through the reservoir zone defined by the interpreted horizons. The preserved window was from top reservoir +10ms to base reservoir -10ms. The only data affected by this operation are those outside this window.

3.2.3 – Spectral matching

After exponential gain correction, amplitude spectra for each angle stack for both vintages were calculated in order to ensure that both vintages had similar spectral characteristics. In order to limit the bias in the 4D AVO inversion results, it is desirable to have amplitude spectra similar enough that a single set of wavelets can be used for each seismic vintage. If a sufficient spectral similarity is not observed between the two vintages, a spectral matching was applied to match the higher amplitude spectra to the lower.

3.2.4 – 3D seismic warping

3D seismic warping accounts for travel time and/or imaging differences as a result of velocity changes in the reservoir due to steam injection. As noted in Chapter 2-1, steam injection can lower seismic velocities up to 30% (Batzle et al., 2004). Without correcting for these velocity changes, baseline and monitor events through the steamed zone will be improperly aligned and thus unsuitable for 4D AVO inversion. The 3D seismic warping algorithm used in this study computes displacements in time as well as in-line and x-line directions to compensate for the differences in positioning of reflection events due to changes in velocity. The seismic warping was performed by first estimating a smoothly varying dynamic displacement field in time and the in-line and x-line directions to maximize the cross-correlation of events between the seismic data volumes. To compensate for any possible polarity reversals between angle-stacks, the Hilbert transform is used to compare the energy envelope. Displacements are computed in an iterative fashion to ensure maximum similarity between sub-stacks going into the warping. Subsequently, the cumulative displacement field is applied to correct for any travel time and/or imaging differences between vintages. The alignment for each vintage was performed according to the order shown in Figure 3-2.

$$0°\text{-}13° \longrightarrow 13°\text{-}20° \longrightarrow fullBaseline$$
$$\longleftarrow 20°\text{-}26° \longleftarrow 26°\text{-}31° \longleftarrow 31°\text{-}36° \longleftarrow 36°\text{-}41° \longleftarrow 41°\text{-}45°$$

Figure 3-2: Ordering of warping alignment.

The time and in-line and cross-line shifts between baseline and monitor vintages were computed on the full-stacks to increase fold, thereby ensuring the most consistent comparison possible. In this study, the full-stacks contain data from 5-31 degrees. The nearest angles were excluded due to a large amount of high frequency noise and the farther angles were excluded in an attempt to limit stacking of polarity reversals. Figure 3-3 shows the in-line, cross-line and time displacements between the baseline and monitor full-stacks extracted at the reservoir interval. The displacements are localized to the area of the horizontal well pairs and provide an indication of the areal extent of steam injection related anomalies. Displacements on the survey margins are likely associated with differences in fold distribution between surveys and poor data coverage and are likely unrelated to actual reservoir changes.

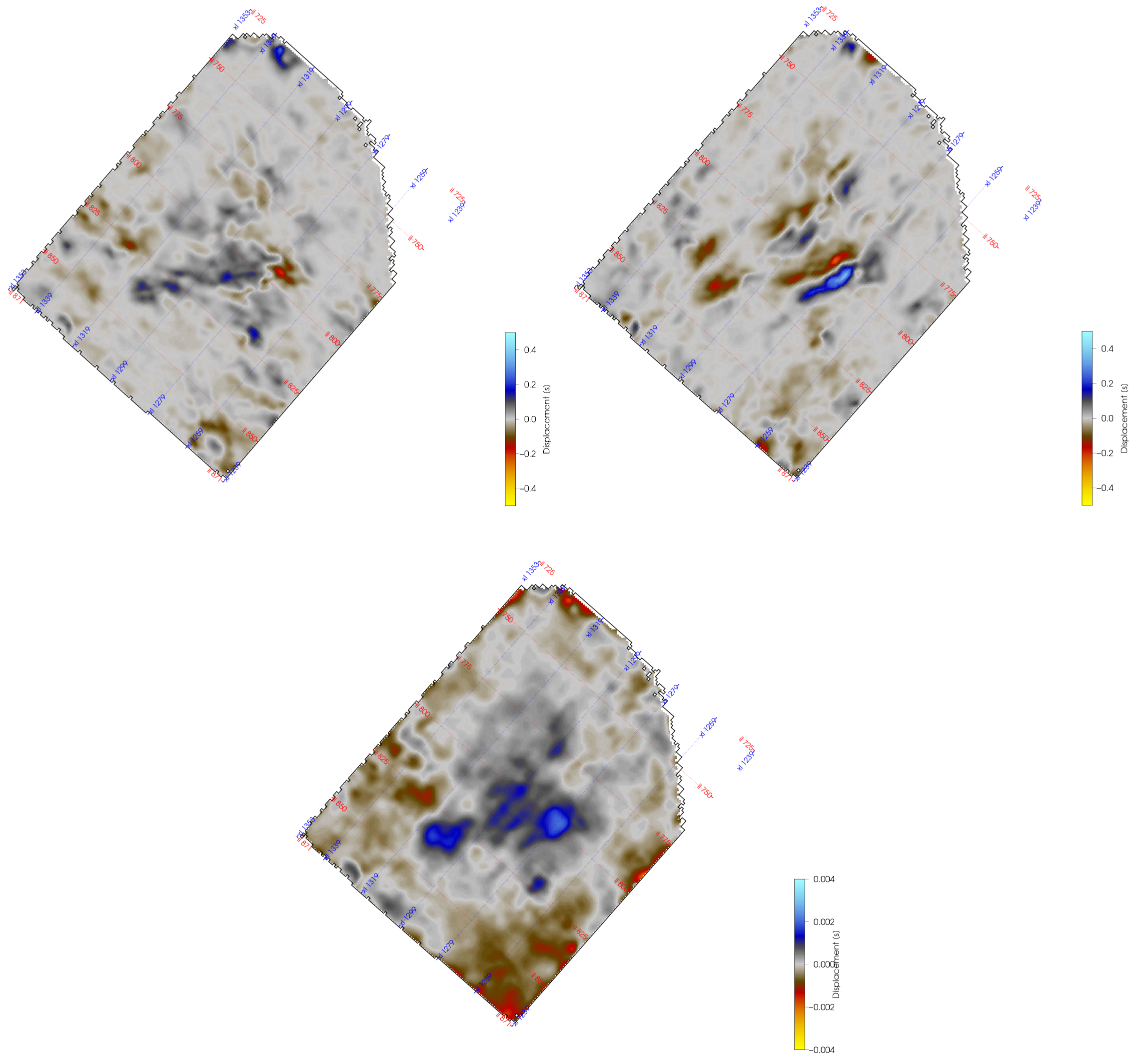

Figure 3-3: Horizon slices through the reservoir zone showing in-line displacement (top-left), cross-line displacement (top-right) and 4D time shifts (bottom).

To ensure that the warp is working properly, seismic difference volumes were calculated using the full stacks from each vintage. Figure 3-4 shows results comparing the difference of the baseline and monitor full-stacks before and after the 3D seismic warping is applied. Before warping there is a characteristic cascaded amplitude difference observed below the area of steaming caused by misalignment caused by the aforementioned velocity changes. After warping this cascaded amplitude difference is minimized indicating that the events are now aligned, resulting in a more readily interpretable difference volume.

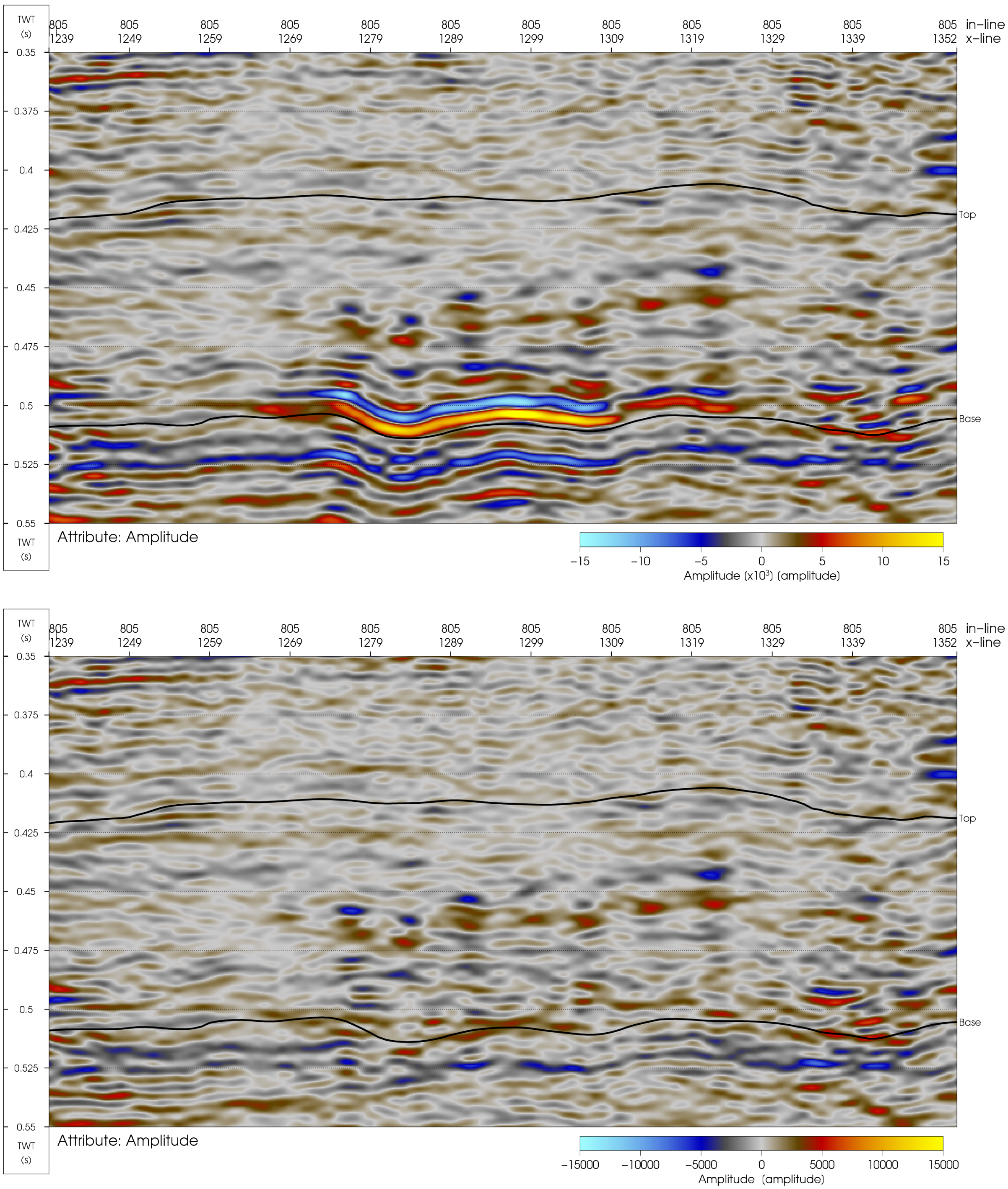

Figure 3-4: In-line cross-sections of full-stack amplitude differences before pre-conditioning (left) after pre-conditioning (right).

Chapter 4 – Relative 4D AVO Inversion

4.1 – AVO inversion overview

An inverse problem involves calculating a model from a set of observations. In AVO inversion, the idea is to calculate the elastic model of the subsurface that produced the angle-dependent reflection amplitudes observed in seismic data. In this case, an Aki-Richards (1980) inversion kernel, a linearized version of the Zoeppritz equations, was used to compute the angle-dependent reflectivities. The Aki-Richards approximation is given by

$$R(\theta) = \frac{1}{2}\left(1 - 4\frac{\bar{\beta}^2}{\bar{\alpha}^2}\sin\theta^2\right)\frac{\Delta\rho}{\bar{\rho}} + \frac{1}{2}(1+\tan\theta^2)\frac{\Delta\alpha}{\bar{\alpha}} - 4\frac{\bar{\beta}^2}{\bar{\alpha}^2}\sin\theta^2\frac{\Delta\beta}{\bar{\beta}}, \tag{11}$$

where $\bar{\alpha}, \bar{\beta}, \bar{\rho}$ are the average P-wave, S-wave and density across an interface and θ is the average of the incident and transmission reflection angles.

In this study, the pre-stack partial angle-stacks were inverted directly for changes in acoustic impedance, Vp/Vs and density. The 4D pre-stack AVO inversion is based on a time-lapse AVO inversion algorithm using the Aki-Richards three-term reflectivity model. I performed the inversion using Qeye software, which is a model-based, global simultaneous AVO inversion algorithm the inverts all input seismic stacks simultaneously for all three parameters. The software uses a simulated annealing algorithm that is capable of locating the global minimum of a given function. This differs from gradient descent based methods that converge to local minima. The algorithm used in this study calculates a pseudo-hessian from the data residuals as a model update. As such, if local minima are a problem, the applied algorithm is more accurate, but more computationally expensive than gradient descent methods. The number of iterations for the model updating can be varied, but the algorithm has a fast cooling schedule thus more than 3 iterations generally does not change results. The specifics of the inversion algorithm are beyond the scope of this study, proprietary to Qeye and I took no part its design or implementation.

The inversion allows for parameterization in any meaningful combination of elastic parameters (acoustic impedance, shear impedance, Vp/Vs ratio, density, etc.) and does not use any constraints dictating the relationship between parameters. As such, it truly inverts for each parameter simultaneously and independently. The parameterization choice of acoustic impedance, Vp/Vs and density was chosen over acoustic impedance, shear impedance and density as Vp/Vs ratio is a more directly related to changes in lithology than AI and SI. Inverting for AI and SI generally yields better correlations to well logs thus giving the impression of a better inversion result, but this masks the fact that it is the ratio of these two parameters that most strongly relates to lithology change. To provide a more direct indication of inversion quality, Vp/Vs ratio was inverted for directly.

The objective function that is mathematically minimized consists of three terms. The first term is the spatial mean squared misfit between observed and synthetic seismic; the second term is the spatial mean squared misfit between inverted model and prior model; the third term is a penalty on horizontal variation of the inverted model. All of these terms are inputs into the objective function to be minimized using the simulated annealing algorithm and their respective weights can be adjusted as part of inversion testing. For the 4D AVO inversion, multi-vintage pre-stack seismic data are inverted directly for ratio changes with each vintage treated equally as shown in the following equations from Nasser et al., 2016:

$$\begin{aligned} Z_1 &= Z_0 + \Delta Z_1, \\ Z_2 &= Z_0 + \Delta Z_2, \\ \Delta Z_1 + \Delta Z_2 &= 0, \end{aligned} \tag{12}$$

where Z_n is the logarithmic impedance of the nth vintage and Z_0 is a mean model. This formulation is symmetric with respect to any given vintage, meaning that there is no bias toward any particular choice of baseline vintage. The outputs of the inversion are absolute 3D AVO inversion results for each vintage and 4D ratio changes expressed as the ratio of the monitor divided by the baseline survey. For example no change corresponds to a value of 1.0, a decrease of 10% corresponds to a value of 0.9 and an increase of 10% corresponds to a value of 1.1.

Previous 4D AVO inversion studies associated with bitumen saturated reservoirs by Mesdag et al. (2015) and Gray et al. (2015), either invert the seismic differences or invert the baseline and monitor surveys separately to create difference volumes for the elastic properties. A shortcoming of this formulation is that it can introduce 4D changes due to noise differences between seismic vintages. In this study, both seismic vintages are inverted simultaneously. An advantage of this approach is an additional step of noise removal through 4D inversion whereby non-AVO compliant differences are not inverted.

4.2 – Wavelet estimation

Seismic to well tie is a fundamental step in seismic interpretation. Various methodologies of deconvolution are used to extract wavelets from seismic data. As shown in equation 11, a properly calibrated AVO inversion uses angle-dependent reflectivities to calculate elastic properties. In order to obtain true reflectivities from the data, we must first extract angle-dependent wavelets to be used as inputs to the AVO inversion to deconvolve the background AVO response from the processing. For this project, the three well logs were used to extract multi-well wavelets using the Blackman-Tukey (1958) method, where the solution is optimized in the least-squares sense for all wells. The Blackman-Tukey method extracts an optimal, smooth least-squares wavelet with no constraints on amplitude or phase.

In addition to estimating wavelets using the Blackman-Tukey method, another methodology was implemented that will be referred to as the Q-attenuation method based on the work described by Cho et al., 2011. In this method, a reference near offset wavelet is evolved in angle using phase shifts and spectral attenuation calculated directly from the seismic. The obvious advantage of this method is its non-reliance on potentially inaccurate shear log data, which was discussed in Chapter 2-5. If we re-arrange the Aki-Richards equation to the intercept (A), gradient (B) and curvature (C) formulation, the equation becomes the following

$$R(\theta) = A + B\sin\theta^2 + C\sin\theta^2\tan\theta^2, \qquad (12)$$

where $A = \frac{1}{2}\left(\frac{\Delta\alpha}{\bar{\alpha}} + \frac{\Delta\rho}{\bar{\rho}}\right), B = \frac{1}{2}\frac{\Delta\alpha}{\bar{\alpha}} - 4\frac{\bar{\beta}^2}{\bar{\alpha}^2}\frac{\Delta\beta}{\bar{\beta}} - 2\frac{\bar{\beta}^2}{\bar{\alpha}^2}\frac{\Delta\rho}{\bar{\rho}}, C = \frac{1}{2}\frac{\Delta\alpha}{\bar{\alpha}}$ we can see that the only term with a dependence on the shear log is the gradient (B). If we differentiate equation 12 with respect to shear wave velocity we obtain the following

$$dR = \sin\theta^2\, dB, \qquad (13)$$

which shows that given an error in shear wave velocity, errors in the angle dependent reflection coefficient has a sine squared dependence with angle. This suggests that near angle wavelet estimation should be relatively unaffected by shear log errors, but far angle wavelets will become progressively more biased. The Q-attenuation wavelets therefore represent a more conservative approach to angle dependent wavelet estimation as they only require well log input data for the near angle reference wavelet.

The Q-attenuation wavelets are referred to as such because they use basic constant Q attenuation theory as the core of the methodology. Constant Q theory is based upon the following equation for frequency dependent amplitude decay with time

$$A(f) = A_0(f)e^{\frac{-\pi f t}{Q}}, \tag{14}$$

where A_0 is a reference amplitude, f is a frequency, t is time and Q is quality factor. If we combine $\frac{t}{Q}$ to yield a new quantity, referred to as K, we can linearize and re-arrange equation 14 to yield

$$\ln \frac{A(f)}{A_0(f)} = \ln e^{-\pi f K} = \ln \frac{A(f)}{A_0(f)} = -\pi f K, \tag{15}$$

and solve for K via a least squares solution of the following

$$\mathrm{A} = FK\,, \qquad K = (F^T F)^{-1} F^T A\,, \tag{16}$$

where A, F and K are matrices. Once we have found a value for K, we can apply it to equation 14 to evolve the amplitude spectrum of the reference wavelet. The wavelet phase was evolved by computing a constant phase change between the reference seismic angle stack and the subsequent angle stacks using the following equation

$$\varphi_i = \varphi_0 + \varphi_{diff}, \tag{17}$$

where $\varphi_{diff} = \tan \frac{Imag(F(A_0(f_{peak})))}{Real(F(A_0(f_{peak})))}^{-1} - \tan \frac{Imag(F(A_i(f_{peak})))}{Real(F(A_i(f_{peak})))}^{-1}$, where F is the Fourier transform and f_{peak} is the peak frequency.

Numerous sets of angle-dependent wavelets were extracted for testing in both 3D AVO inversion and well tie tests. Various single and multi-well wavelets were estimated using varying combinations of the four supplied wells to optimize the wavelet estimation to the most reliable and well behaved well log and seismic data. The resulting wavelets are subsequently cross-validated by applying each wavelet to each well and calculating the resulting correlation and misfit values. The results of this wavelet cross-validation experiment are shown in Figure 4-1.

This plot shows the correlation and misfit for each wavelet tested for the reference 13-20 degree angle stack and as an average calculated for all partial stacks. The bars indicate the overall statistics while individual well statistics are plotted as symbols according to the legend. These plots provide an initial list of candidate wavelets to be used in subsequent inversion testing. Based on these plots, it was decided to run test inversions using multi-well wavelet 2 and the Q-attenuation wavelets as these wavelets have relatively high correlations without being biased to poor quality log data or short logging intervals. These two candidate sets of wavelets are shown in Figure 4-2. Plots of well ties for two wells for the near angle stack using Q-attenuation wavelets are shown in Figure 4-3.

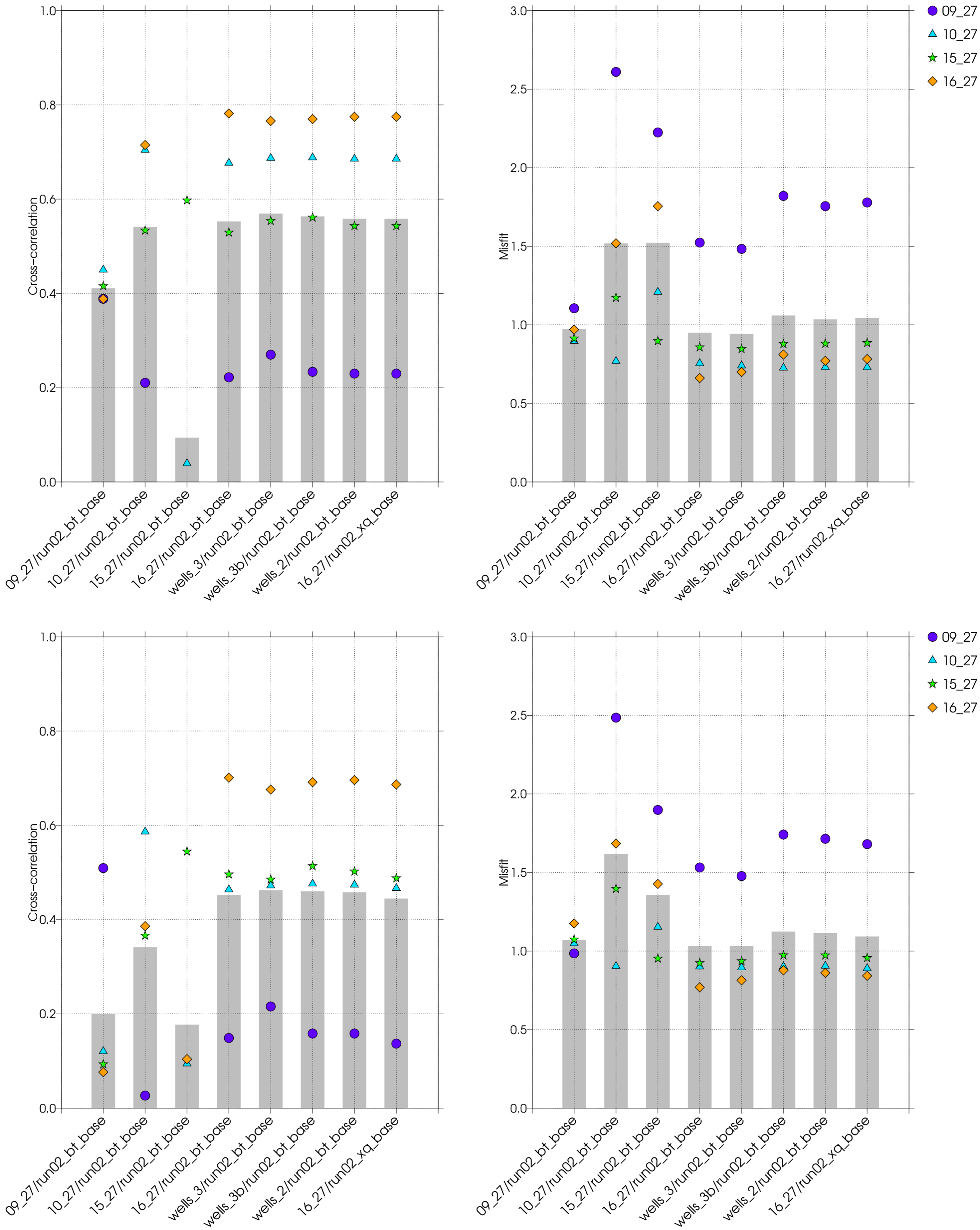

Figure 4-1: Wavelet cross validation statistics for reference stack (top) and all stacks (bottom)

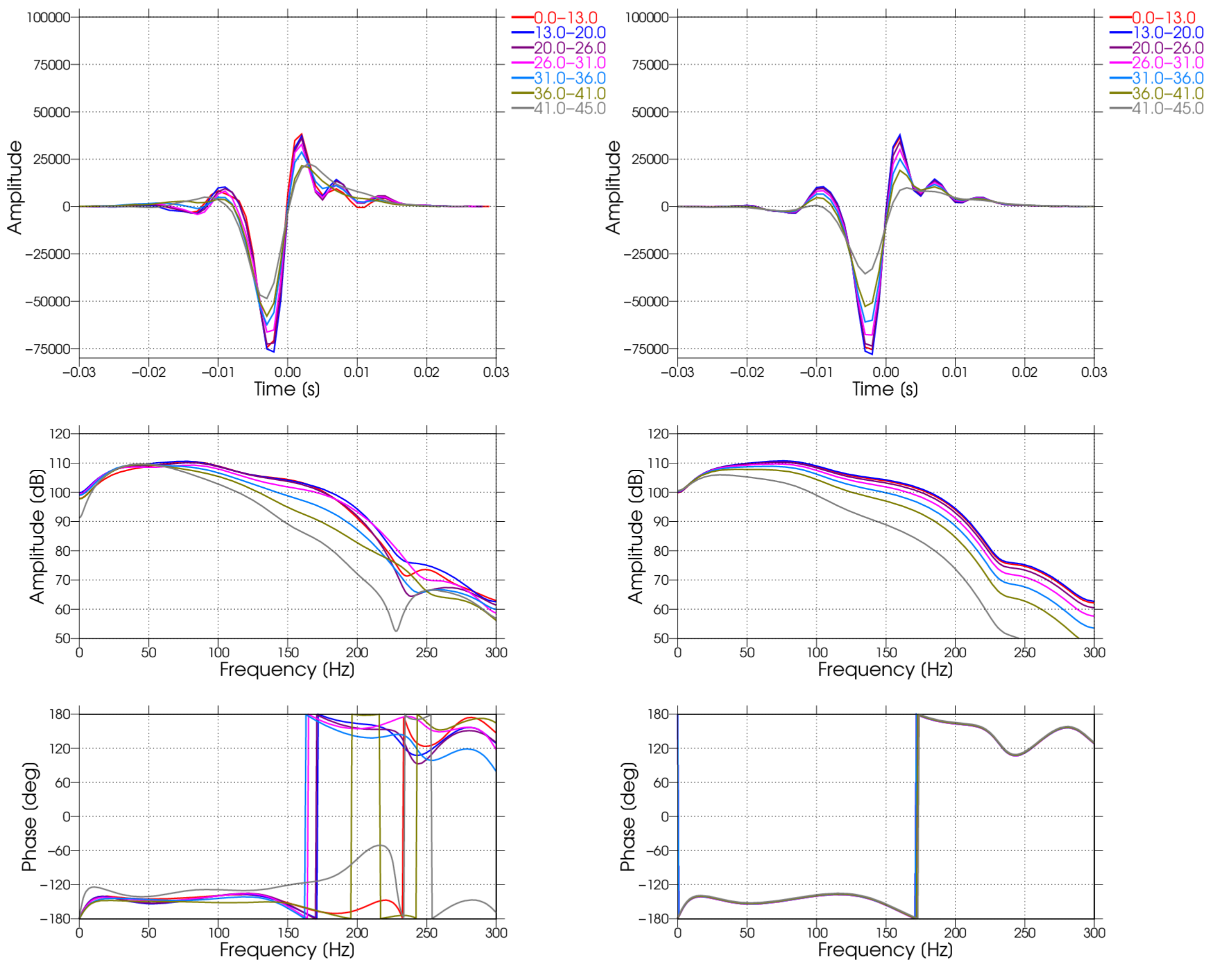

Figure 4-2: Multi-well 2 (left) and Q-attenuation (right) angle-dependent wavelets extracted from seismic angle stacks.

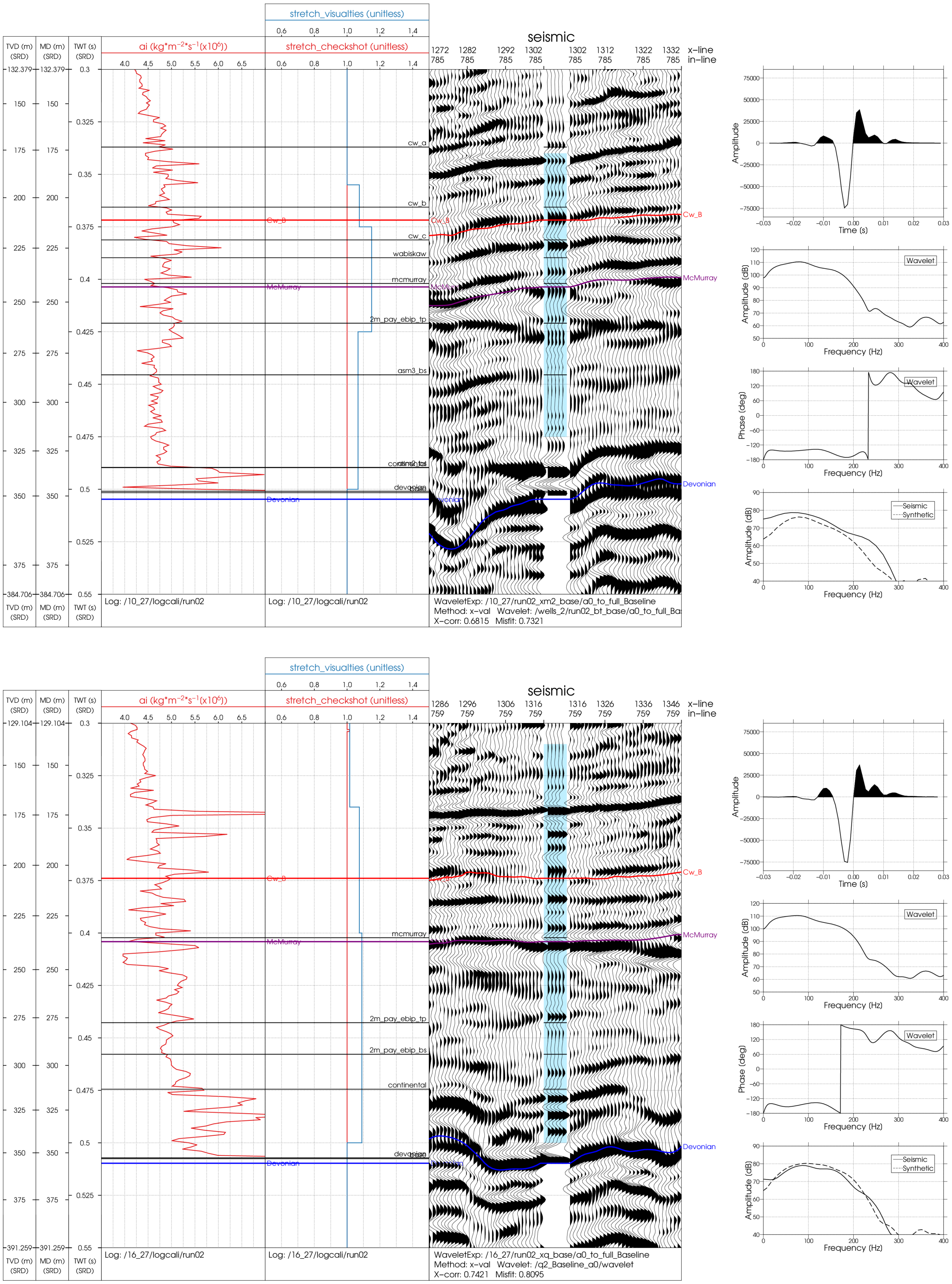

Figure 4-3: Seismic to well ties for two well for near offset angle stack using Q-attenuation wavelet.

4.3 – Signal to noise ratio

Data acquired specifically to enable AVO analysis in the study area resulted in far offsets being available, thus allowing for the creation of angle stacks up to 45 degrees. The 45-degree angle stacks have coherent, continuous events and a high fold in excess of 50 through the central portion of the study area, but suffer at survey edges where similar offset and azimuth coverage is not available. This results in low-fold and low signal to noise ratios in these areas. In addition, differences in acquisition between the baseline and monitor surveys resulted in differences in offset coverage that manifest as significant differences in data quality and availability at the survey boundaries. Mean fold distribution maps through the reservoir zone for the 41-45 degree angle stack for each vintage are compared in Figure 4-4. 4D AVO inversion incorrectly identifies these differences due to acquisition as real subsurface change. The resulting elastic changes are therefore contaminated at the survey boundaries and inhibit proper interpretation over the entire survey area.

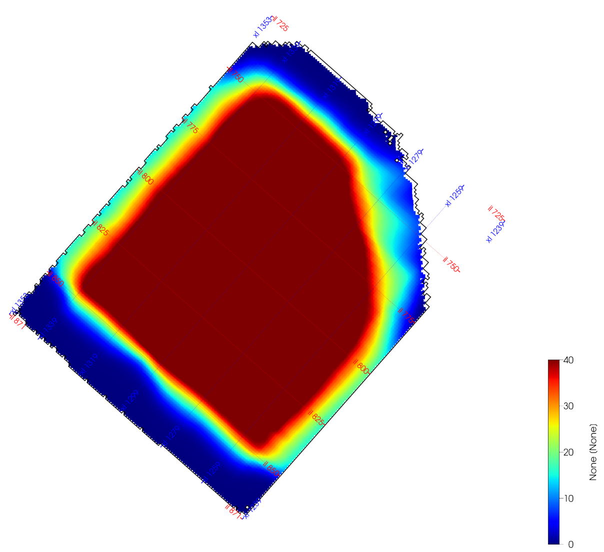

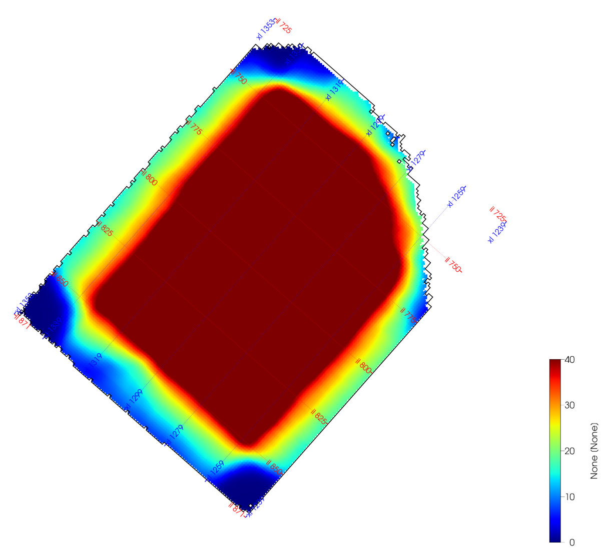

Figure 4-4: Mean fold distribution for the 41-45 degree angle stack through the reservoir zone.

To limit the impact of these differences on the final inversion results, signal to noise ratio volumes were calculated for each angle stack of each vintage from the fold volumes according to the following equation

$$SNR = \sqrt{fold}. \tag{18}$$

The resulting volumes for each vintage were then combined into a single signal to noise volume for each angle stack by taking the most pessimistic, or lowest, signal to noise value between the two vintages. These volumes are used as direct signal to noise inputs in the 4D AVO inversion to allow for greater misfit of residual energy where there is low signal to noise ratios. As a result, the 4D anomalies at the survey boundaries caused by acquisition differences are reduced. Map view results of the change in Vp/Vs with and without the inclusion of the signal to noise ratio models are shown in Figure 4-5.

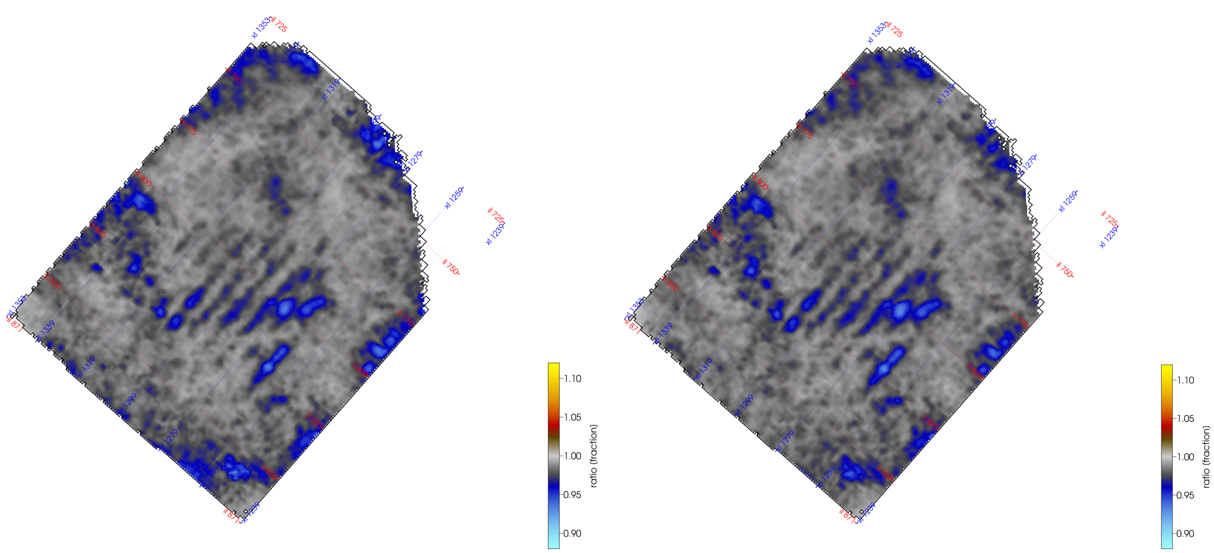

Figure 4-5: Minimum 4D Vp/Vs inversion results extracted through the reservoir zone without (left) and with (right) inclusion of signal to noise volumes.

4.4 – Initial inversion results

Various tests were performed to choose the optimum inversion parameters for this study. Tests included wavelets, angle stack inclusions, horizontal continuity and deviation from prior model parameters. As no 4D calibration data were available, testing was validated by comparing baseline 3D inversion results to well logs. The most important tests were angle stack inclusions and wavelet choice. Testing revealed an improved correlation and sensitivity for Vp/Vs and density when the farthest angle stacks were included. Near stack inclusions were also tested and resulted in the determination that excluding the near stack yields improved Vp/Vs results. The reason for this observation is unclear, but I suggest that the higher frequencies of the near stack, including several events not observed in subsequent stacks, negatively impacted the AVO response of the seismic. The difference in results between the multi-well and Q-attenuation wavelets discussed in Chapter 4-2 were subtle with little to no difference observed in the AI or Vp/Vs results. Because of an improved density response and a perceived improved robustness from reduced bias to well logs, the Q-attenuation wavelets were chosen as the optimal set of wavelets. Ultimately, through thorough testing it was determined that the optimized inversion results favoured using angle stack inclusions from 13-45 degrees and the Q-attenuation wavelets shown in Figure 4-2. For a detailed statistical explanation of the inversion results, please see Chapter 6-1.

The initial inversion results were run using a flat background model for AI, Vp/Vs and density that assumes no change. Using a flat model as a starting model was considered the most unbiased result, but the lack of input 4D low frequency model means that the inversion results will be band-limited. Cross sections of the initial 4D AI and Vp/Vs inversion results are shown in Figure 4-6. The eight well bores are clearly delineated by decreases in AI and Vp/Vs as predicted by rock physics modeling, but these decreases in AI are banded both above and below by increases that are not predicted by the rock physics model. The cause of this observation is discussed further in Chapter 5.

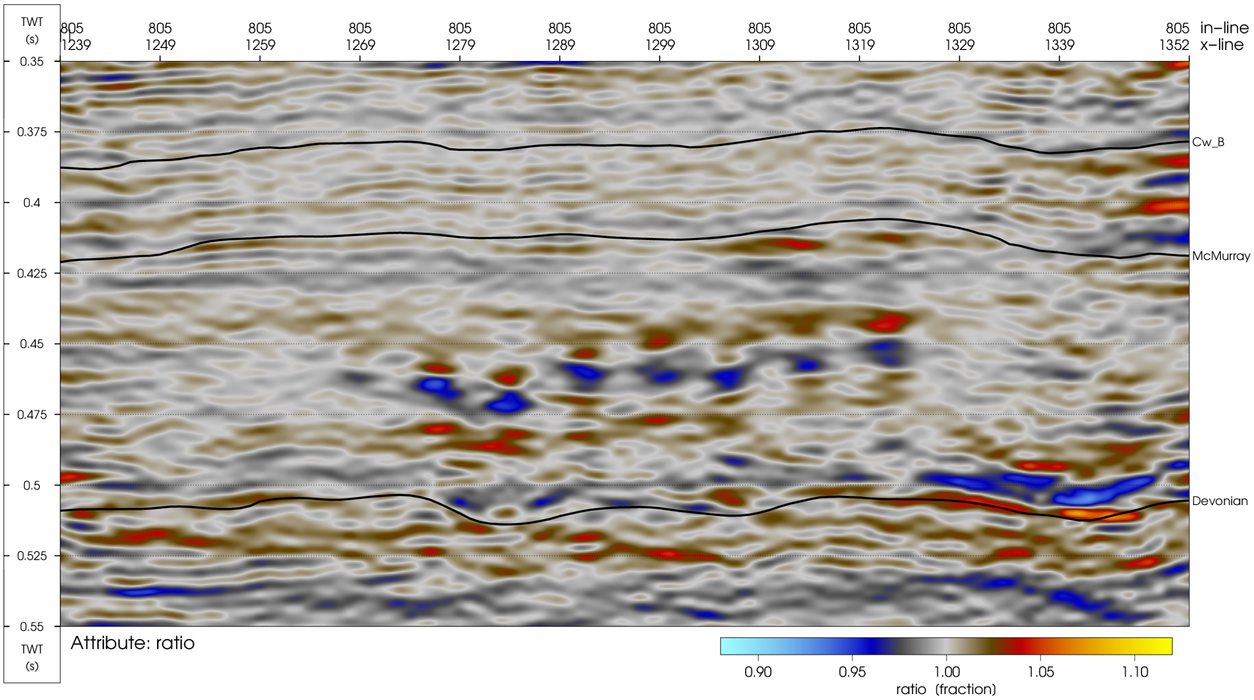

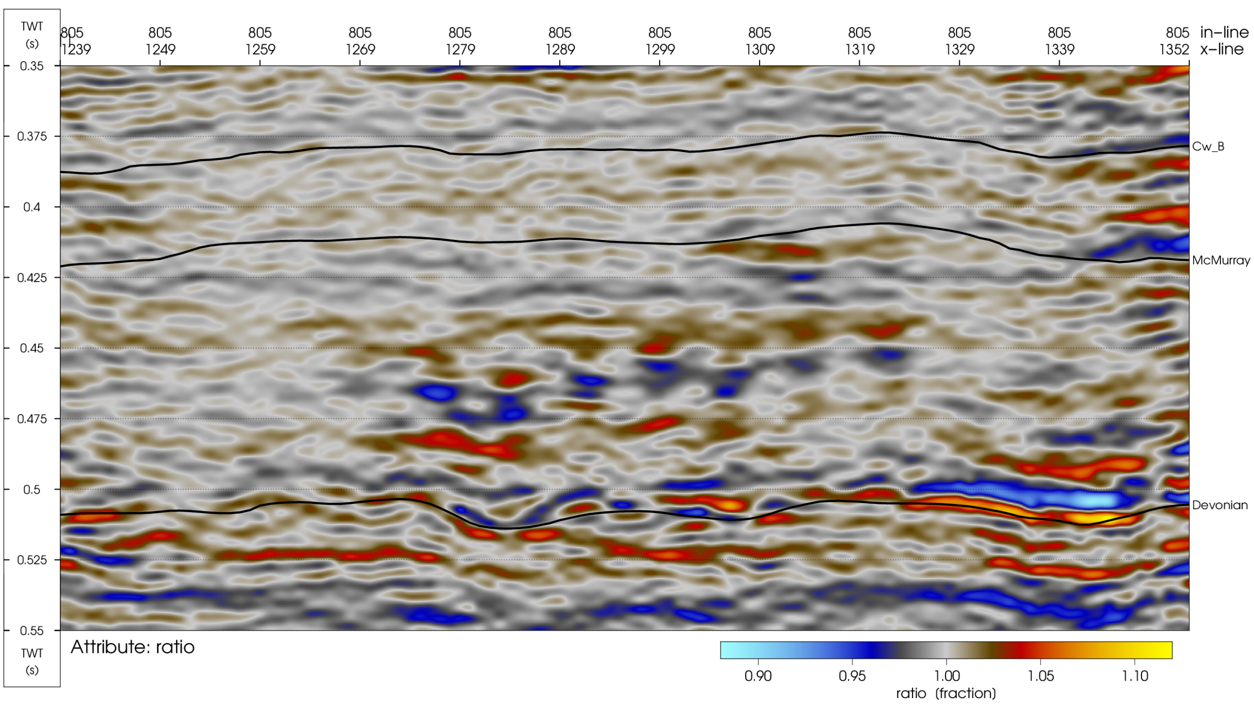

Figure 4-6: Cross sections of initial 4D AVO inversion results for AI (top) and Vp/Vs (bottom) across all well bores.

Chapter 5 – 4D low-frequency modeling

5.1 – Low-frequency modeling overview

Understanding the frequency limitations of the 4D inversion results is an essential step to proper interpretation. In a 3D simultaneous inversion, the missing low-frequency components of our desired elastic properties are typically derived from low-pass filtered well logs extrapolated across the seismic volume using horizons to guide structure. In a 4D sense, one does not typically have access to 4D log data to build a low-frequency model. To minimize the band-limited effects on the inversion results, a low-frequency model must be derived from other means.

Initial 4D AVO inversion results for this study did not use 4D low-frequency models as an input and the interpretability of the results suffered. According to the rock physics model discussed in Chapter 2-4, the 4D response due to steaming is characterized by a decrease in AI due to either a decrease in P wave velocity caused by the Domenico gas phenomena (1976) or a decrease in P and S wave velocity caused by a phase change from bitumen to heated oil. As such, it is expected that surrounding the injection wells where steam has been added to the system, one should see decreases in AI in the inversion results. Interestingly, initial results were characterized by an apparent banding of the expected decreases in AI by increases both above and below. These apparent increases in AI, in addition to not being explained by the rock physics model, are also not corroborated by the time-shifts from the seismic warping. It is expected that if these increase in AI were real, one would see an increase in velocity reflected in the time-shifts, which is not the case. It was therefore hypothesized that the apparent banding are side-lobes associated with the band-limited nature of our seismic signal. In order to gain further insight into this observation, a simple wedge modeling exercise was performed.

5.2 – Wedge modeling

In order to investigate the observations of initial 4D AVO inversion results, a wedge modeling exercise was performed using a predicted time-lapse scenario. The wedge model is intended to replicate the response of an increase in steam saturation, with decreases in both AI and Vp/Vs with no change in density. From this model, two inversions were run. The first convolves the models with a theoretical infinite bandwidth wavelet to create full bandwidth synthetic seismic traces. The second convolves the models with the actual wavelets extracted from this dataset in order to create realistic band limited synthetic seismograms. The results of this wedge modeling exercise can be seen in Figure 4-1. In the full bandwidth solution, the initial models are fully resolved with no leakage or side-lobes present. Conversely, in the band limited solution the same apparent banding is observed that is present in initial inversion results. The results of this exercise, combined with a lack of explanation from rock physics modeling and a lack of corroborating evidence from time-shifts supports the interpretation that the increases in AI observed in the results are due to a lack of low-frequencies in the seismic signal. To remedy this shortcoming and ultimately improve the 4D AVO inversion results, we need to create 4D low-frequency models to fill in the missing low frequencies of the signal.

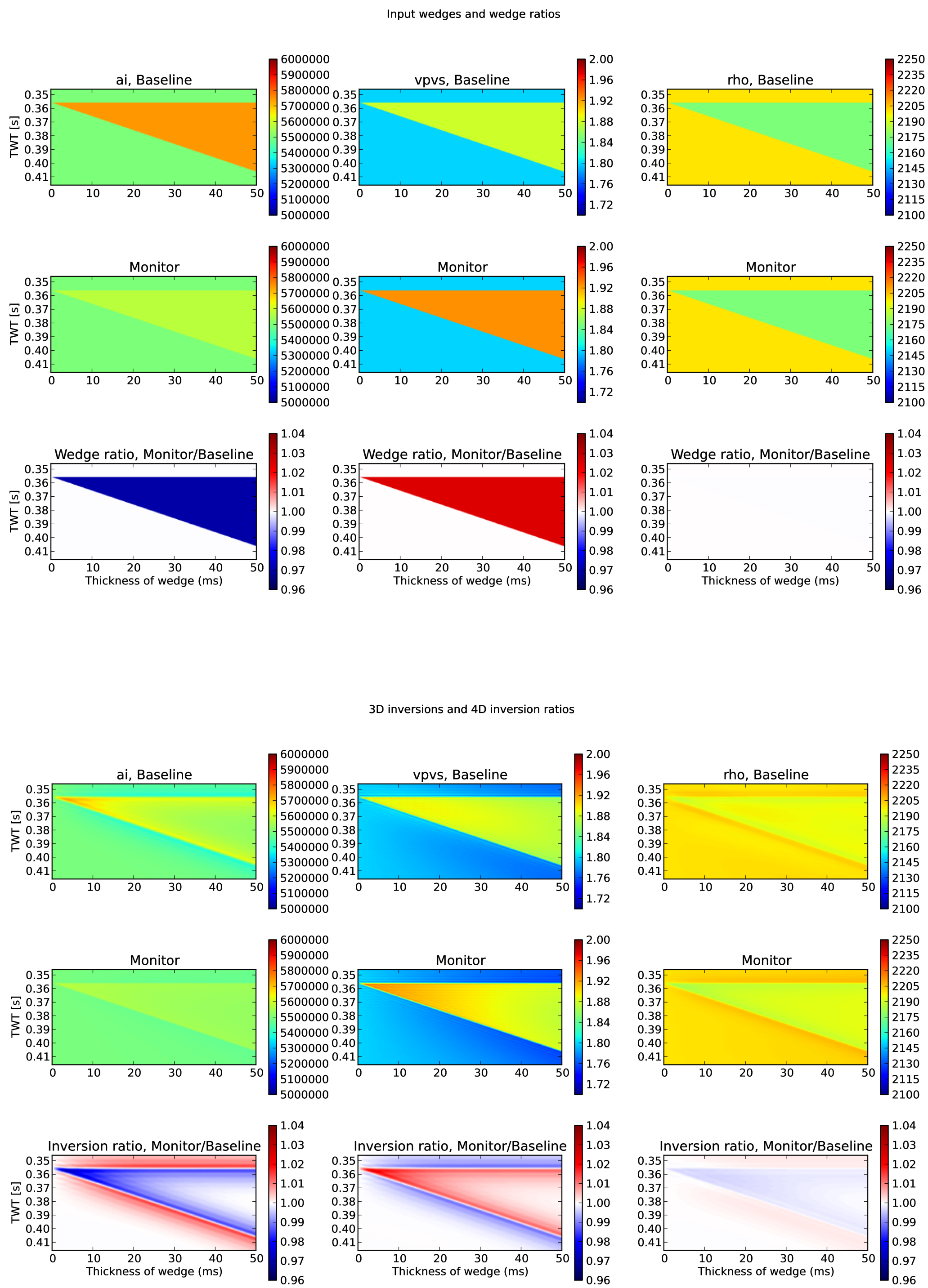

Figure 5-1: Full bandwidth (top) and band-limited (bottom) inversion results for a time-lapse heated oil response.

5.3 – 4D low frequency modeling

Nasser et al. (2016), Gray et al. (2016) and Zhang et al. (2016) among others have described deriving a 4D acoustic impedance low frequency model by differentiating the 4D time-shifts obtained when aligning seismic vintages. Differentiating the time-shifts creates a 4D acoustic velocity volume. This field can then be used as a 4D low frequency model for AI under the assumption of a non-compacting reservoir (Nasser et al. 2016). For this project, I can be reasonably confident that this assumption holds through the zone of interest as pressure maintenance under steam injection prevents the effects of compaction. The time-shift volumes for this project were converted to 4D AI low frequency models by the following equation

$$\frac{Vp_{monitor}}{Vp_{baseline}} = \frac{1}{1+dt_{shift}}, \qquad (19)$$

where dt_{shift} is the derivative of the time shift between baseline and monitor surveys discussed in Chaper 3-2. Cross sections through the reservoir zone of the time-shifts and resulting acoustic velocity change are shown in Figure 5-2. The acoustic velocity change is represented as a relative change from baseline to monitor survey expressed as a ratio. A value of 1.0 indicates no change, a value less than one indicates a decrease in velocity and a value above one indicates an increase in velocity.

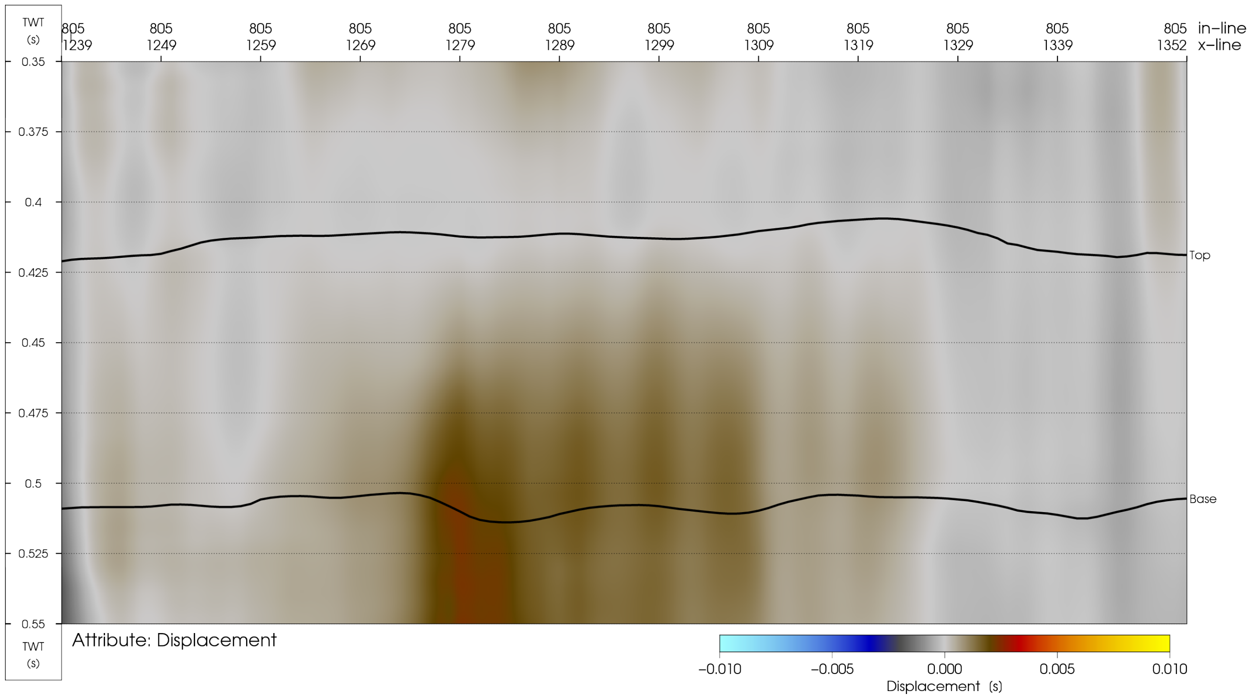

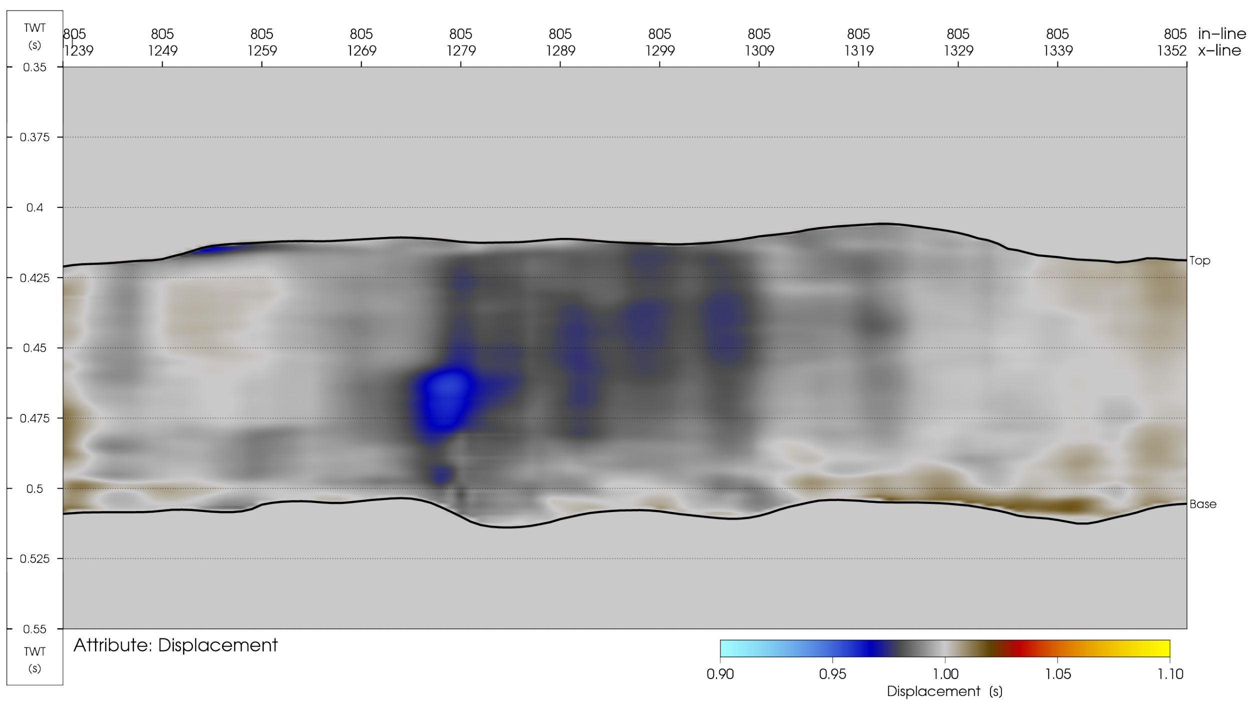

Figure 5-2: Computed time-shift (top) and acoustic velocity change (bottom) from baseline to monitor.

Gray et al. (2016) and Zhang et al. (2016) among others have demonstrated how differentiated 4D time-shifts of 3C PP and PS data from seismic warping are combined to obtain velocity changes, which, under the assumption of a non-compacting reservoir, can be used to obtain 4D low-frequency models for both AI and Vp/Vs. Unfortunately, converted wave PS data is costly to acquire and process therefore PS data is often not acquired. This being the case for my study, a Vp/Vs low frequency model must be recovered by some other means.

Mesdag et al. (2015) applied a simple, linear interpolation on inversion results between interpretations for top and bottom of steam chamber to create 4D low frequency models for AI and Vp/Vs. The drawbacks to such a methodology are 1) interpretation of top and bottom of steam chamber is time consuming and subjective in nature; and 2) this method allows only for linear variation and does not account for potential layering of events such as heated oil lying both above and below the steam chamber as the SAGD process predicts. Nasser et al. (2016) applied a cross-correlation based approach, wherein cross-correlations between relative 4D AVO AI and SI inversion results and change in acoustic velocity are calculated and used to condition the acoustic velocity field in order to create a 4D Vp/Vs low frequency model. The level of bias in the model is then calibrated using monitoring data as the cross-correlation volumes are qualitative in the context of impedances. Both of these methods were tested for use in this study, but the results were unsatisfactory. A new workflow was created taking a similar approach to that of Nasser et al. (20016).

For this study, a simple, binary facies classification on relative inversion results was employed to derive a 4D Vp/Vs low-frequency model using only PP data. Rock physics modeling in Chapter 2 demonstrated that the expected time-lapse changes for both AI and shear impedance (SI) to be decreases from baseline to monitor. It follows that increases observed in the relative inversion results are a consequence of the band-limited nature of the signal. I make use of this knowledge by applying a simple probablistic event classification in SI vs. AI space to separate the relative 4D inversion into steam (decrease in AI and Vp/Vs) and oil (decrease in AI and increase in Vp/Vs). Data falling diagonally across from this classification, for instance an increase in both AI and Vp/Vs for steam, are considered lobe energy and grouped into the same classification. The resulting probability density functions are shown in Figure 5-3. These probability density functions were created by convolving every relative 4D inversion point with a Gaussian distribution function in 2D. Data falling within the “noise” polygons is not predicted in the rock physics model and is therefore given a value of 1.0, meaning no change, in the low frequency model to limit bias while not forcing the results to fit into the simple binary classification scheme.

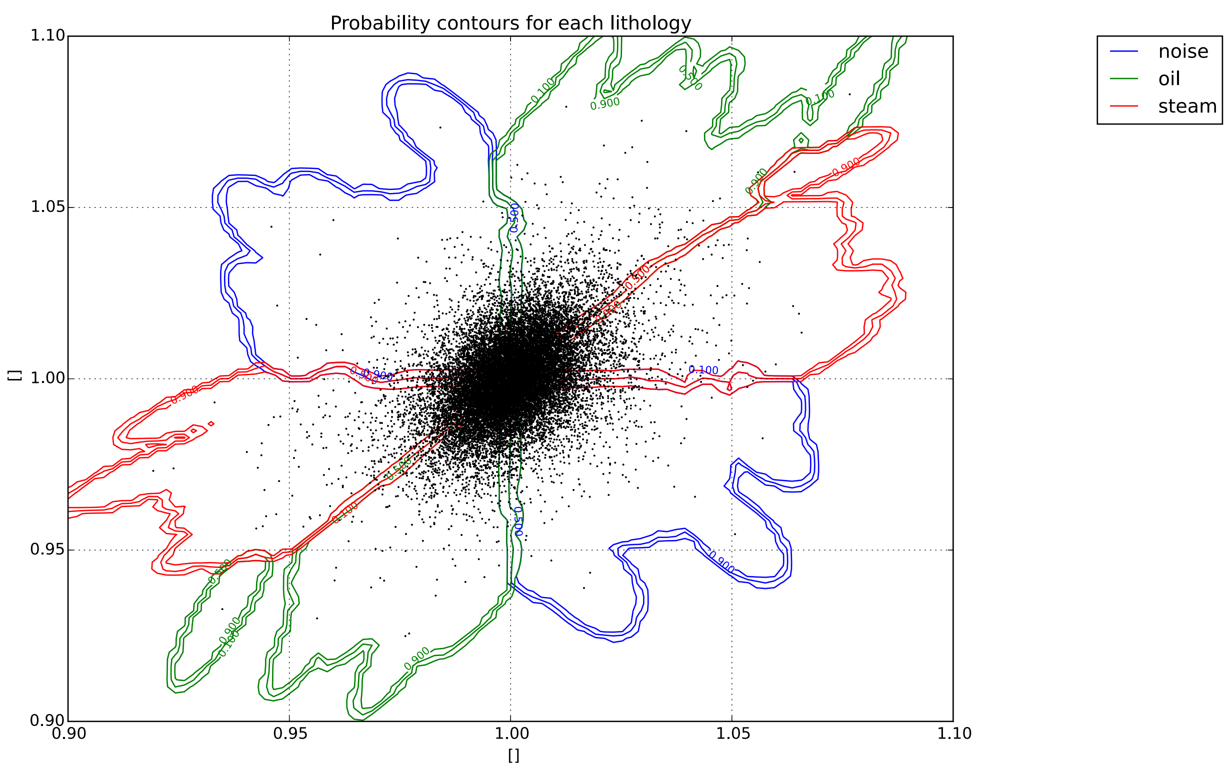

Figure 5-3: Event classification of relative inversion results in SI vs AI space.

Once this classification is applied to the relative inversion results, the probabilities were used in conjunction with the acoustic velocity change to yield the 4D Vp/Vs low frequency model using the follow formula

$$\frac{V_p}{V_s} = Prob_{steam} * \frac{1}{2-\partial V_p} + Prob_{oil} * (2 - \partial V_p), \tag{20}$$

where $Prob_{steam}$ and $Prob_{oil}$ are the steam and oil probabilities produced by applying the classification scheme from Figure 5-3 to the inversion results and ∂V_p is the acoustic velocity change shown in Figure 5-2. If production or monitor data were available, it should be used to calibrate the bias of the resulting model, but unfortunately, no such data were available for this study. A cross section across all well bores of the resulting 4D Vp/Vs low frequency model is shown in Figure 5-4. The resulting field seems to have a similar shape to those of the SAGD schematic in Figure 1-2, with increases in Vp/Vs (possibly indicative of heated oil) surrounding the decreases in Vp/Vs (possibly indicative of increase in steam saturation). The correlation between the expected SAGD shape and geometry and those observed in this volume provides a qualitative indication that the 4D Vp/Vs low frequency model is realistic.

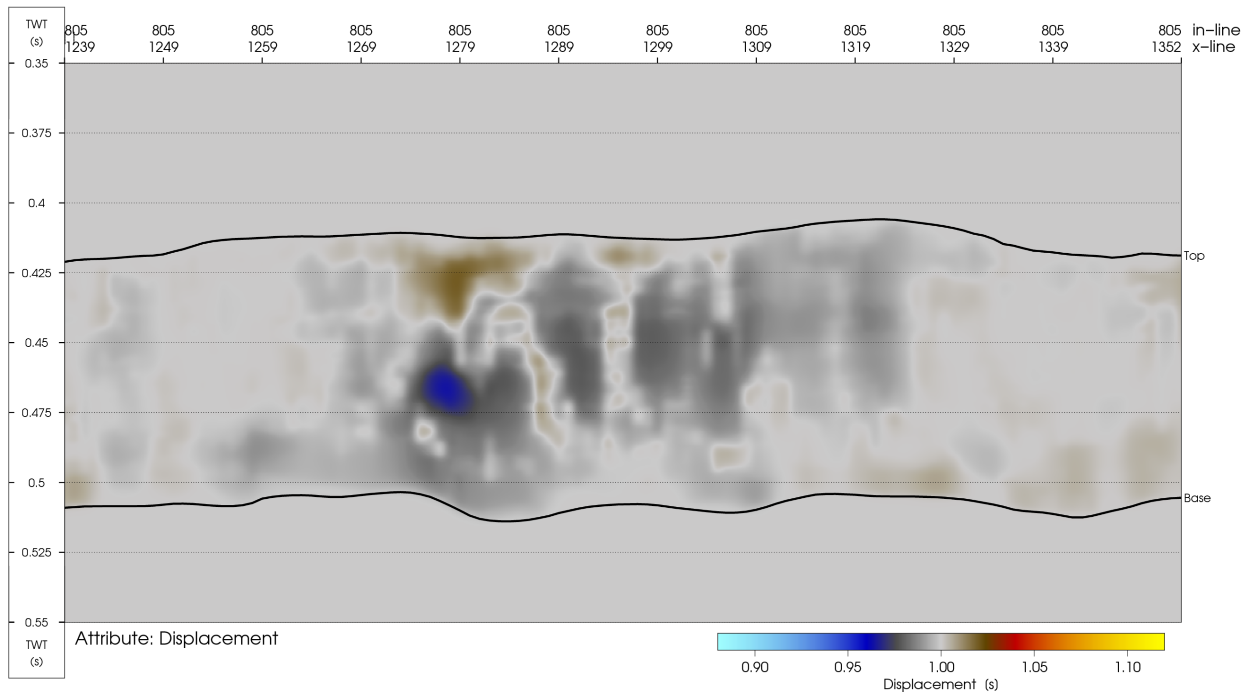

Figure 5-4: Cross section on 4D Vp/Vs low frequency model.

Chapter 6 – 4D rock physics inversion

6.1 – 4D absolute AVO inversion

With the creation of the 4D AI and Vp/Vs low frequency models described in Chapter 5, all the necessary elements for the final 4D AVO inversion are in place. The inclusion of the 4D low frequency models fill the low frequency information missing from the seismic data to give a more realistic, accurate inversion result. Cross sections of the final 4D AI and Vp/Vs AVO inversion results are shown in Figure 6-1. Compared to initial results show in Figure 4-6, the apparent increases are now limited and the interpretability of the results is improved.

There are several key uncertainties affecting the interpretation of the 4D AVO inversion results. In 3D AVO inversion studies, results are validated and error is quantified by comparing inversion results to well control. For this project, I do not have access to any 4D log data for calibration or monitor/production data of any kind. As such, there is some level of uncertainty attached to the optimum inversion inputs and parameter choices. These choices are therefore largely informed by 3D absolute inversion tests and analysis of seismic synthetics and residuals produced during the inversion.

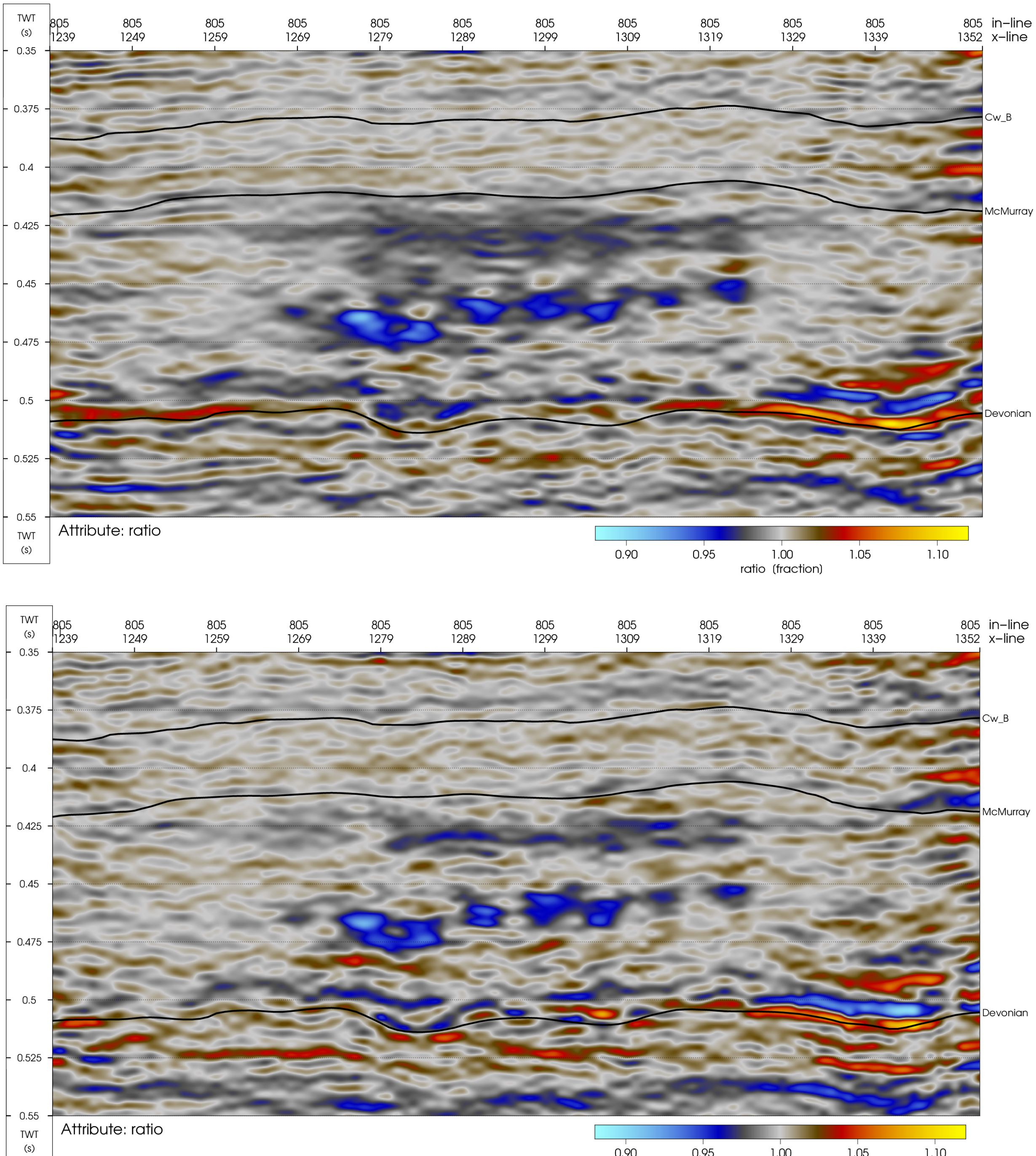

Figure 6-1: Cross sections of final 4D AVO inversion results across well bores.

The choice of optimum 3D inversion results was based primarily upon statistics calculated between the inversion results and available well log data and to a lesser extent, visual inspection. Final 3D AVO inversion results for AI, Vp/Vs and density are all considered acceptable. The results for Vp/Vs ratio have the highest degree of uncertainty due to the lowest correlation values between baseline inversion results and well logs. The inclusion of the farthest angle stack resulted in marginal improvements in correlation for both Vp/Vs and density results with a marginal decrease in correlation for AI. Ultimately, it was decided that a marginal sacrifice in AI accuracy for improved Vp/Vs and density characterization was optimal. Figure 6-2 contains cross-plots of AI, Vp/Vs and density statistics for the optimized 3D AVO inversion run. The number of points plotted for each parameter is not equal as not all log intervals were the same. The correlations between inversion results and well logs using all wells for AI, Vp/Vs and density are 0.781, 0.579 and 0.664, respectively. Table 4 shows the correlations, covariance and slope for each parameter for each well. Figure 6-3 compares inversion results to well logs with mini in line sections for two wells. Without any 4D calibration data, it is assumed that the inversion that yields the optimum baseline 3D inversion results will also yield the optimum 4D inversion results. The only source of 4D validation available was a qualitative assessment of the spatial correlation between the location of horizontal wells and 4D inversion results, which were very consistent.

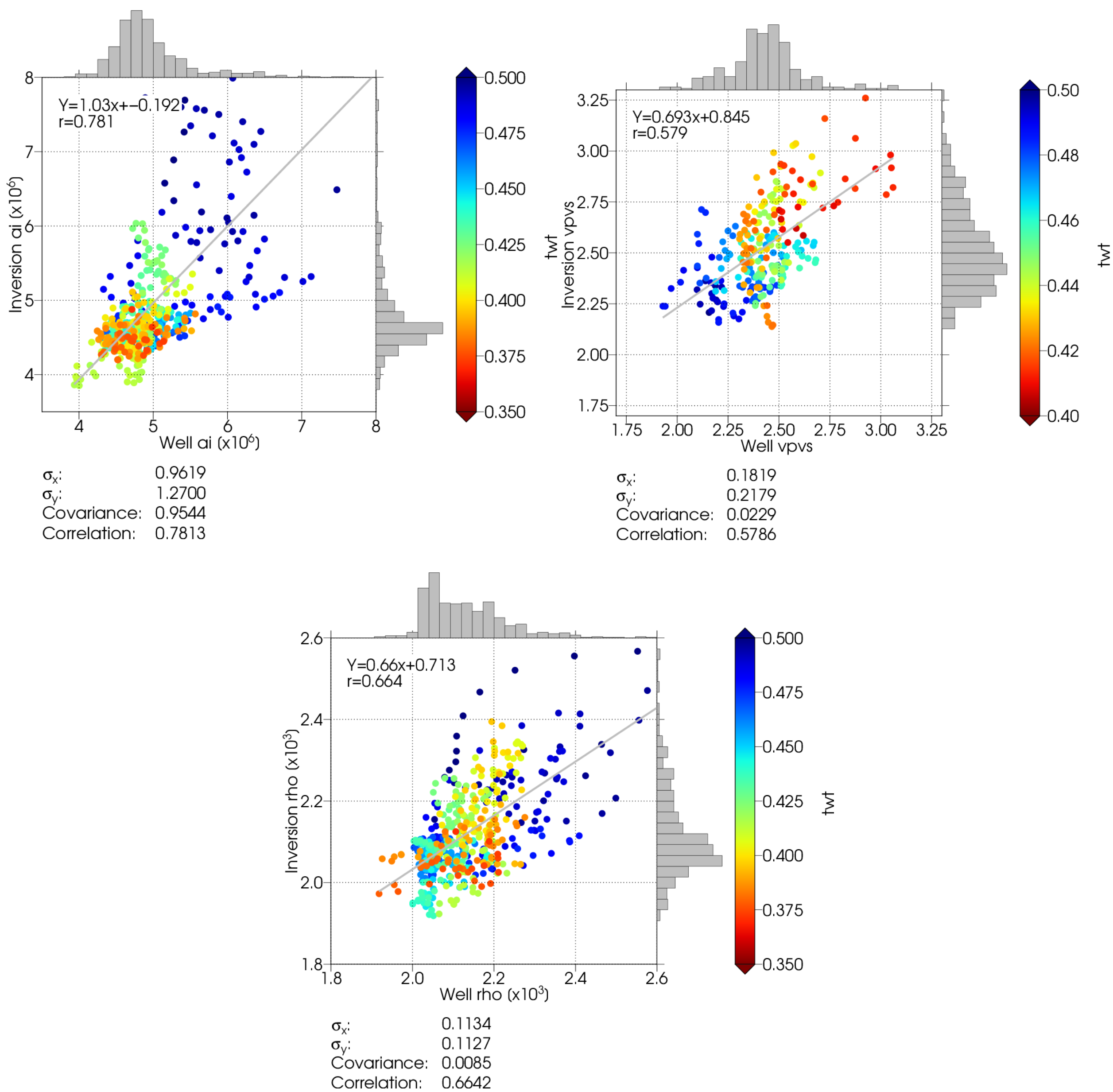

Figure 6-2: Crossplots of inversion vs. well logs with statistics for AI (top-left), Vp/Vs (top-right) and density(bottom).

Table 4: Statistics for 3D AVO inversion results

Well	AI Corr	AI Covar	AI Slope	Vp/Vs Corr	Vp/Vs Covari	Vp/Vs Slope	Density Corr	Density Covar	Density Slope
1	0.84	0.4072	0.517	0.44	0.0184	0.356	0.49	0.0044	0.373
2	0.80	1.4423	1.06	0.66	0.0446	0.453	0.59	0.0084	0.718
3	0.87	1.1248	1.26	0.39	0.0264	0.244	0.80	0.0117	0.757
4	0.85	0.7652	1.05	0.47	0.0206	0.705	0.75	0.0091	0.755
Total	0.78	0.9544	1.03	0.579	0.0229	0.693	0.66	0.0085	0.66

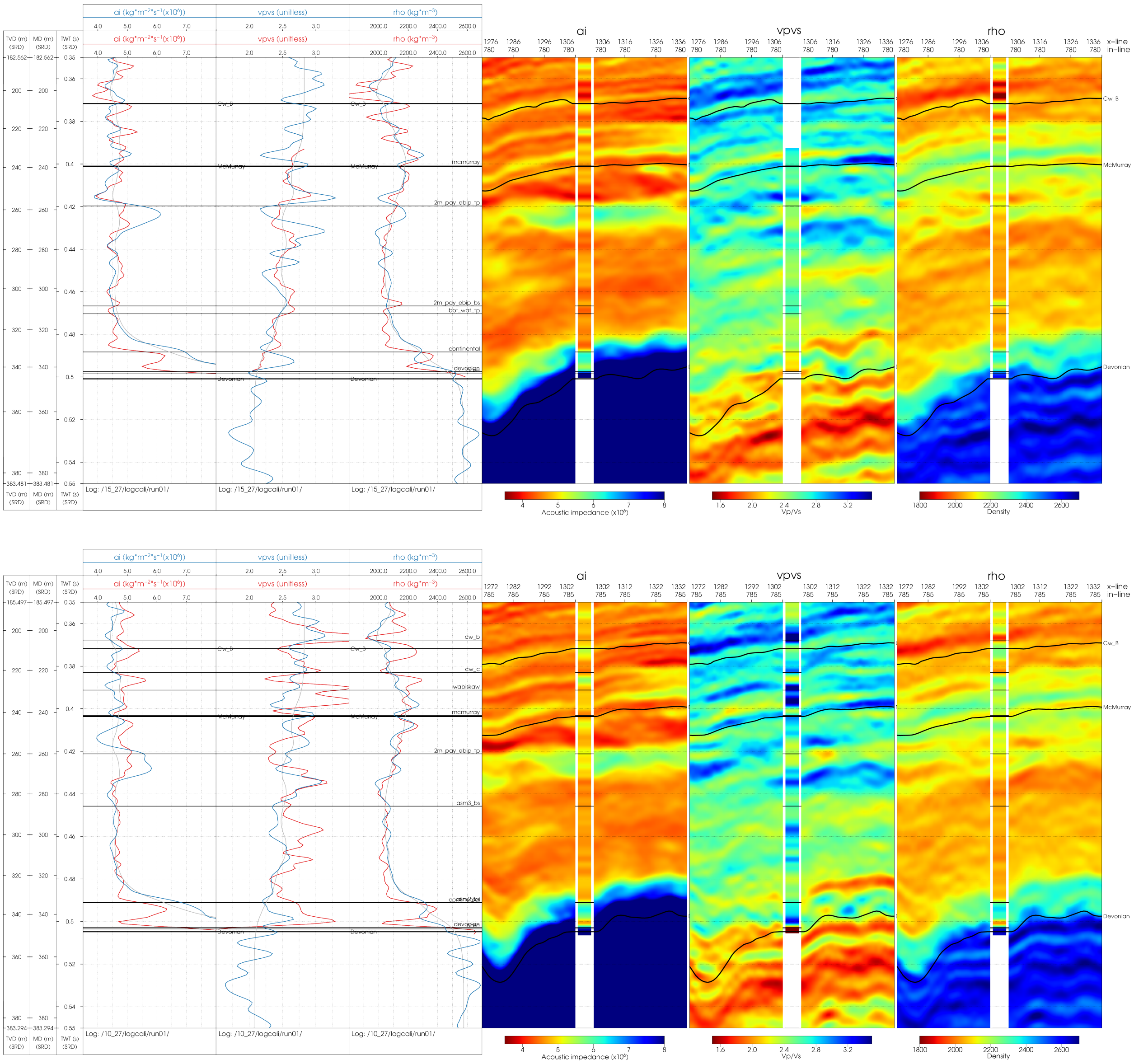

Figure 6-3: Baseline AVO inversion results (blue) vs. well logs (red) with mini-inline sections.

These optimized 3D inversion results were validated based on a combination of visual inspection and statistical analysis, but the inclusion of far angle ranges such as the 41-45 degree angle stack carries an additional risk in 4D AVO inversion due to an associated lack of repeatability. The farther angle ranges correspond to increased travel times and longer ray paths in the subsurface. These longer ray paths are more prone to possible noise, which is inherently not repeatable. In theory, inverting both vintages simultaneously in a 4D AVO inversion will ignore non AVO compliant noise in the data, thereby limiting this problem, but if any 4D noise does carry an AVO signature it will be modeled and impact the results. This potential uncertainty in the final 4D AVO inversion results was weighted against the uplift in 3D results seen by including the farthest angle stack and it was ultimately decided to use all the data available understanding the possible issues associated with the decision.

6.2 – Rock physics inversion

Using the 4D rock physics model and the 4D AVO inversion results, a subsequent 4D rock physics inversion was performed the inverts directly for changes in petrophysical parameters. This inversion is performed in order to further mitigate interpretation ambiguity by transforming the inverted geophysical properties into more immediately interpretable petrophysical quantities that are intuitive to multiple disciplines including geology and engineering. This final step is key to producing results that can be used immediately to update a reservoir model by delineating steam development and mobile oil, leading to production optimization opportunities. Justyna et al. (2015) discuss how knowing the areal distribution and saturation of injected fluids can mitigate early steam breakthrough, allowing for optimized OSR (oil-to-steam ratio) and improved project economics.

Optimum rock physics inversion parameter testing was accomplished in a similar manner to the 4D AVO inversion results. Tests included deviation from prior parameters and adding soft correlations between petrophysical parameters calculated from petrophysical well log data by calculating a covariance matrix. Once again as no production or monitoring data were available for validation of 4D results, these tests were assessed based on the match between baseline 3D rock physics inversion results and petrophysical well logs. The background models used for the rock physics inversion were flat models with starting values shown in Table 5. The starting model for porosity is a relatively low value as the rock physics model uses the re-normalized logs described in Chapter 2.3. This porosity corresponds to the 100% water saturated porosity in the formation, which is low due to the high volume of bitumen.

Table 5: Starting values for 4D rock physics inversion

Water saturation	Steam saturation	Oil saturation	Volume of bitumen	Volume of shale	Porosity
0.95	0.05	0.05	0.30	0.20	0.10

As no oil or steam saturation are present in the baseline 3D rock physics inversion, only the porosity, volume of shale and volume of bitumen rock physics inversion results were able to be optimized to well logs. Results for porosity and volume of bitumen are considered acceptable, but results for volume of shale are unconvincing. Overall correlations between 3D rock physics inversion results and petrophysical well logs for all wells were for porosity, volume of shale and volume of bitumen were 0.71, 0.42 and 0.70, respectively. Figure 6-4 shows the statistics for these three properties colour coded by travel time and Figure 6-5 shows inversion results compared to well log values with a mini in line section.

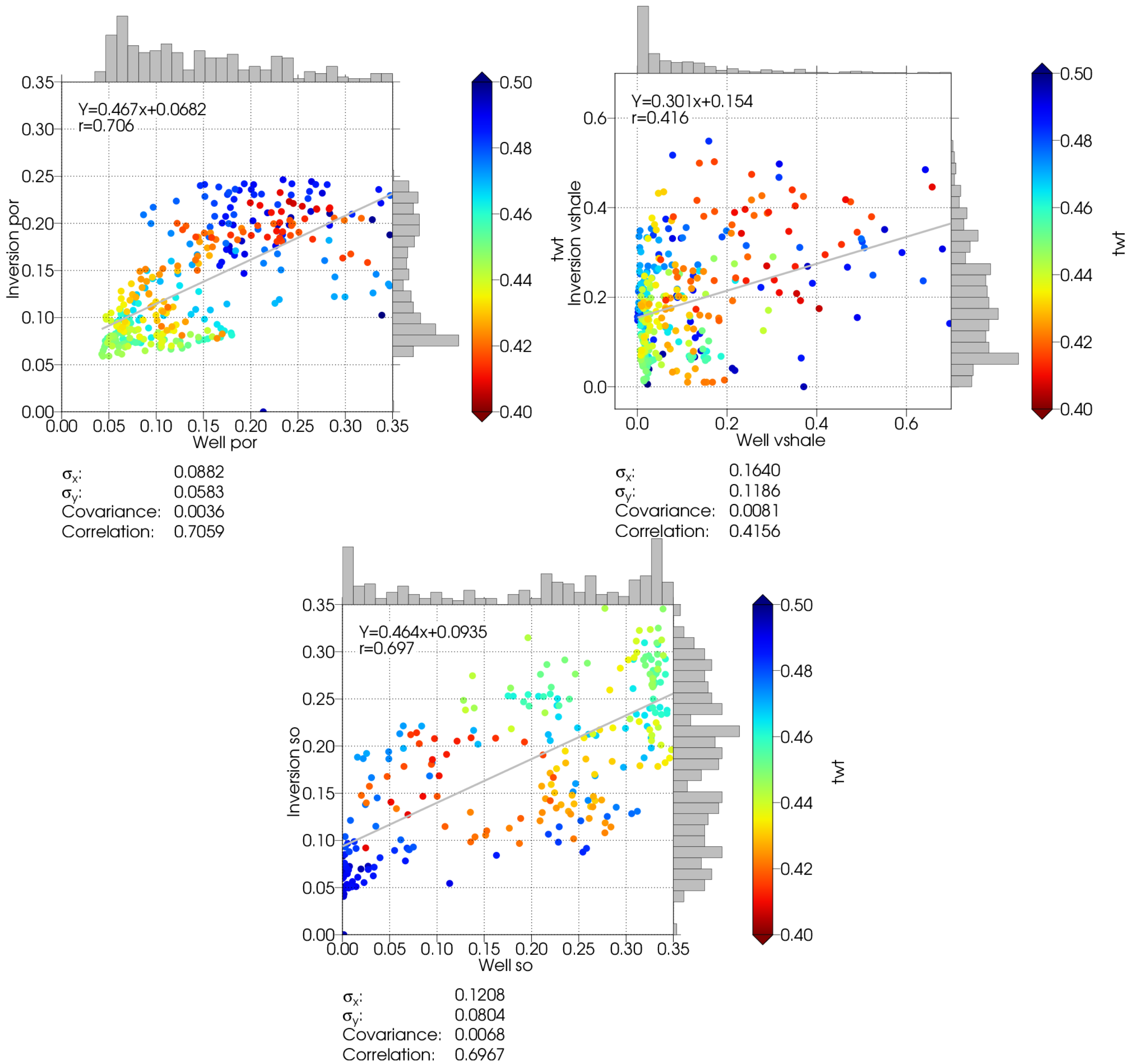

Figure 6-4: Crossplots of inversion vs. well logs with statistics for porosity (top-left), volume of shale (top-right) and volume of bitumen (bottom).

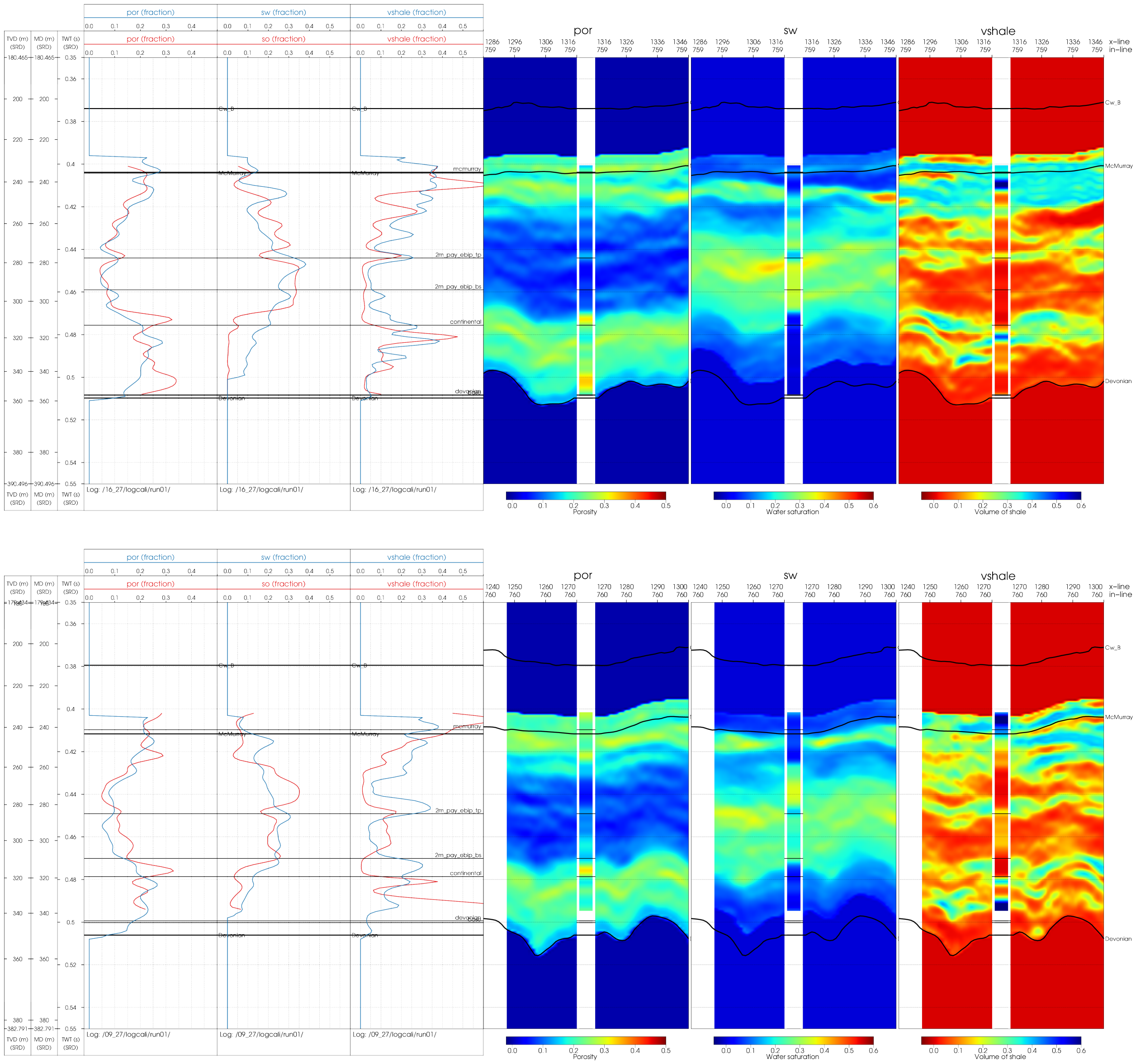

Figure 6-5: Baseline rock physics inversion results (blue) vs. well logs (red) with mini-inline sections.

In order to mitigate the inherent non-uniqueness of estimating 6 petrophysical properties using 3 elastic properties, an a priori covariance matrix was calculated from well log data and used as a soft constraint in the rock physics inversion. Several hard constraints were also used in the time-lapse sense to constrain the solution to make physical sense with the thermal heavy oil process. For instance, it is assumed that the baseline volume of shale 3D rock physics inversion result will be unchanged. Similarly, I assume that the change in porosity is equal to the change in volume of bitumen.

4D rock physics inversion results characterizing changes in oil and steam saturation are shown in Figures 6-5 and 6-6. In Figure 6-5 the variability in the steam and oil content distribution through the reservoir is shown in map view. This variance can be used as input to a reservoir model to optimize areas of both low or high steam chamber development and production. From these images the heterogeneity in the reservoir is observable, and quantifiable in terms of actual fluid changes. In the steam saturation map, all eight well bores are visible, but there are large variations in steam distribution along these well bores. Well bores through the center of the survey show good connectivity all along the well path, while wells on the east and west show poor connectivity, possibly identifying baffles suppressing steam chamber growth. On the west side of the survey, steam chamber development has not yet progressed to the extent of those in the central and eastern parts of the survey and a large amount of steam has accumulated at the toe (to the south) of a western well with little steam being seen elsewhere. On the other hand, in the eastern-most well pairs, one can already beginning to see steam chamber connectivity between well bores.

In the oil saturation map, even more heterogeneity is evident. A significant accumulation of oil is present in the same area as the large connected steam chamber growth along the eastern-most well pairs. There are also indications of heated oil development along certain portions of well bores, but not necessarily directly coinciding with the areas with the most significant steam chamber development. Currently, most of the heated oil accumulations fall along well bores, suggesting that this oil will be produced by the lower producing wells in the future, however if for instance the large accumulation to the eastern part of the survey were to remain present in subsequent surveys, suggesting that this oil is not accessible by producing wells, this accumulation could represent an ideal placement for the drilling of an in-fill well.

Figure 6-6 shows a 3D visualization of the steam and oil saturation changes. In this view the geometry of the changes is similar to those outlined in the schematic SAGD operation shown in Figure 1-2. The steam chambers along the horizontal well bores are surrounded above and below by heated oil that has been conductively heated by the steam chamber growth. Larger volumes of heated oil have formed at the base of the steam chamber as the density contrast between the heated oil and steam/water emulsion causes oil to sink to the bottom of the heated zone where it can be produced by the production wells. The consistency between the geometry observed in the final results and the schematic geometry is convincing and gives further confidence in a qualitative sense that the 4D rock physics inversion is correctly differentiating the fluid changes in the reservoir.

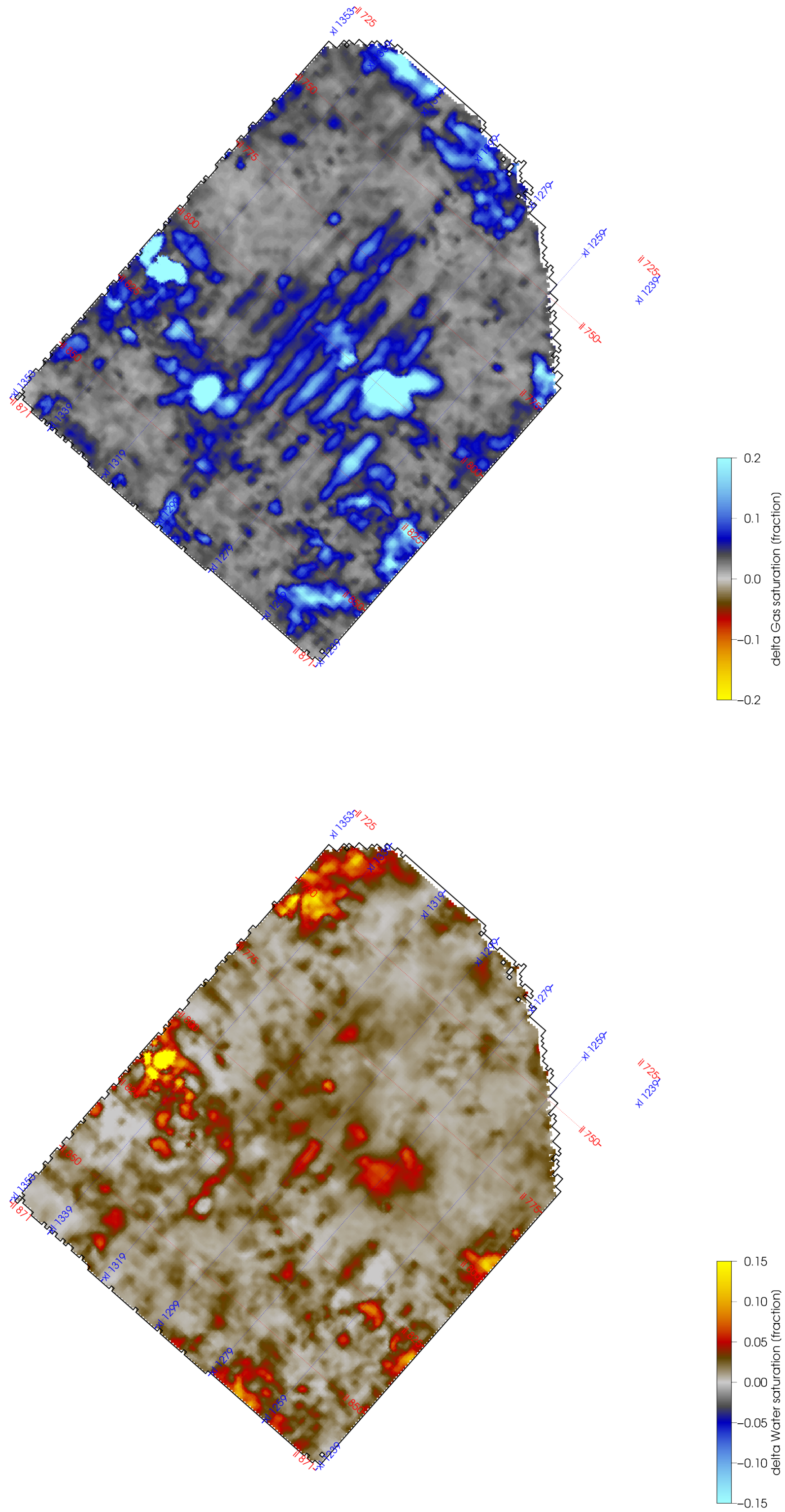

Figure 6-6: Map view of maximum change in steam saturation (top) and oil saturation (bottom) extracted through the reservoir interval.

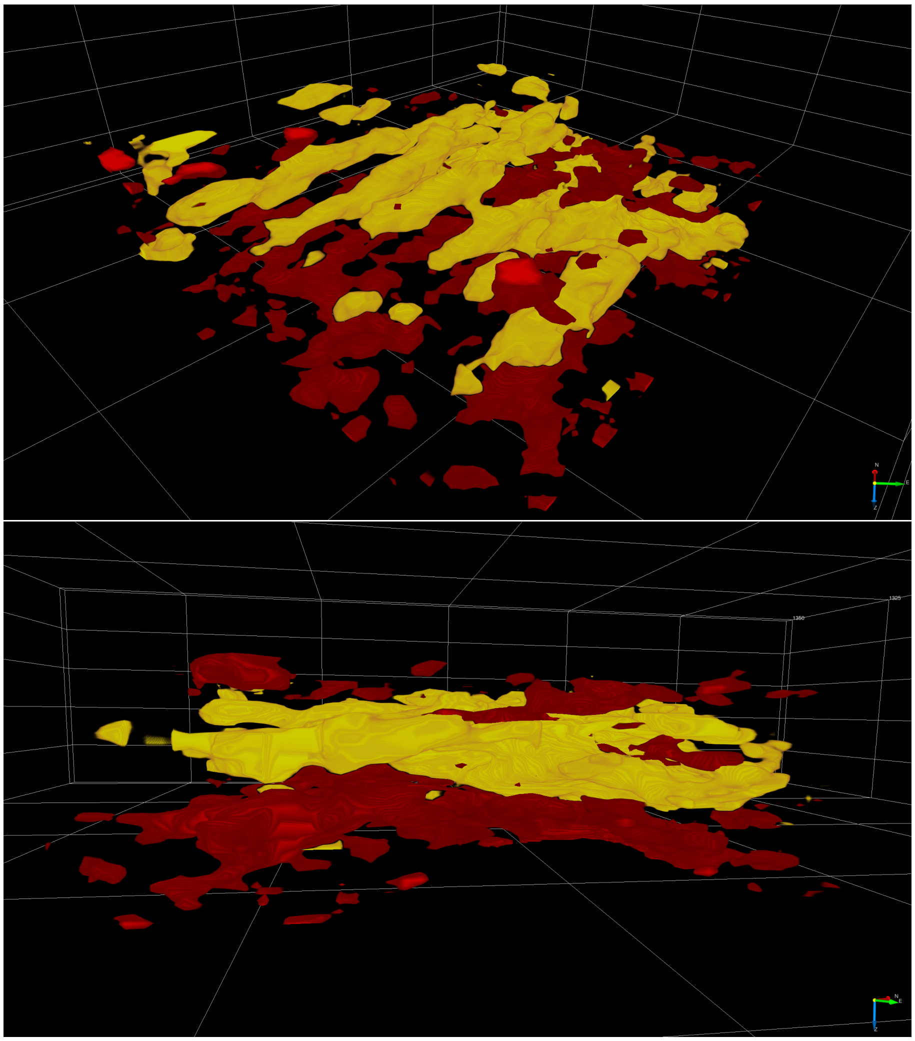

Figure 6-7: 3D views of steam saturation change (yellow) and oil saturation change (red).

6.3 – Geomechanics

In addition to fluid changes, SAGD operations are associated with geomechanical changes that result in changes in elastic properties. In particular, we expect that temperature and pressure changes will also result in and observable seismic response. For the rock physics modeling described in Chapter 2-4 I did not have laboratory or monitor pressure and temperature data, therefore these effects were not included explicitly in the 4D rock physics model and are a source of uncertainty in the inversion results. First order approximations for pressure change were therefore calculated from the velocity changes using simple relationships from Kato et al. (2008) and several simple assumptions.

There are two key assumptions that were made in calculating these geomechanical volumes. As described by Nakayama et al. (2008), the extremely low thermal conductivity of bitumen effectively constrains any temperature changes in the reservoir to only the areas directly surrounding the steam chambers. It follows that any changes observed far away from the steam chambers are therefore caused by pressure changes. With this knowledge, I applied a simple first order, linear approximation relating the velocity change to change in pressure for areas away from the steam chambers. With real laboratory data, a calibrated relationship between these two properties could be derived, but for the purposes of this study, the following experimental equation was used from Kato et al. (2008)

$$V_p = 0.0593 * \log\left(P_{confine} - P_{pore}\right) - 0.375 + V_{p_0}, \qquad (21)$$

where V_{p0} is the reservoir velocity in km/s at in-situ conditions, $P_{confine}$ is the confining pressure and P_{pore} is the pore pressure both in pounds per square inch. The experimental values of these equations can be calibrated if laboratory data were available for the specific field, but for the purposes of this study, this was not the case. As such, Kato's experimental values were used including an initial in-situ velocity of 2.5 km/s. If this value is compared to the logs in Figure 2-4, one can see that this choice is consistent with the well logs in the reservoir from this study suggesting this approximation is reasonable. The value for $P_{confine}$ is approximated using average well log values from the reservoir. Confining pressure can be approximated using a lithostatic pressure gradient and an average density and reservoir depth from the well logs. In this case, $P_{confine} = \rho_{avg} gh = 1800 \frac{kg}{m^3} * 9.81 \frac{m}{s} * 250m = 4.41MPa = 640\ Psi.$ Once these values are obtained, pore pressure can be calculated by re-arranging equation 15 to

$$P_{pore} = P_{confine} - e^{\frac{V_{p_0}(\delta V_p - 1.0) + b}{m}}, \quad (22)$$

A map view of the results through the reservoir zone is shown in Figure 6-8. The results are expressed as pore pressure in mega Pascals. This map shows the extent of pressure development in the reservoir. Compared to the rock physics inversion results in Figure 6-5, the pressure signal has developed well beyond the steam chamber development, but has spatial variability consistent with the steam chamber results with the highest pressure located in areas with the largest steam chamber development. Once again, a limitation with the pressure volume is that the values lose their accuracy closer to steam chambers as the velocity change becomes coupled with the fluid and temperature effects. As such, the volume must be used with care, but is nonetheless an reliable means at delineating the pressure front and is a reasonable first order quantitative approximation away from steam chambers.

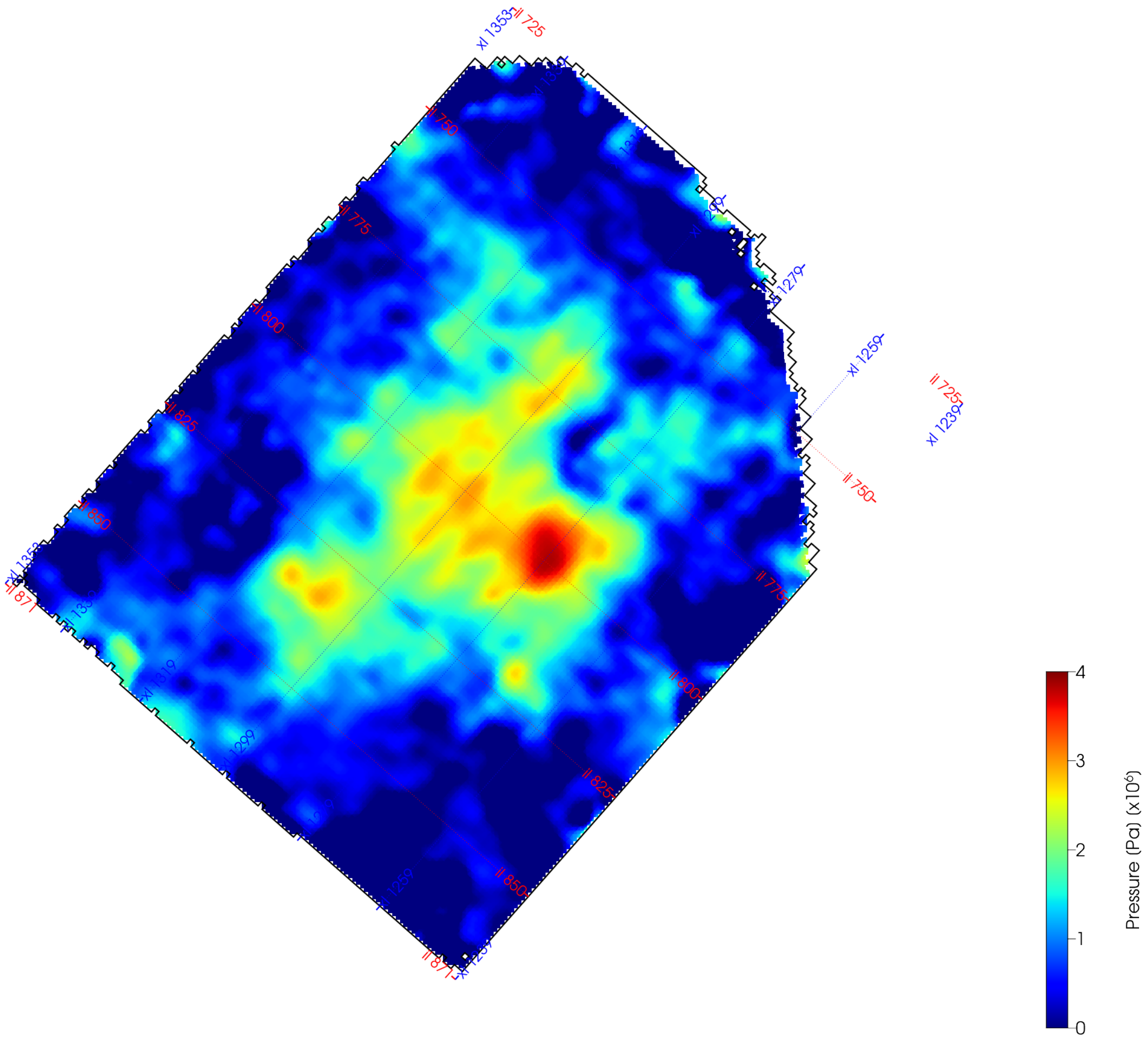

Figure 6-8: Map view of pore pressure change through the reservoir zone.

Chapter 7 – Discussion and Conclusions

The 4D rock physics inversion results shown in this study demonstrate that, in order to properly understand the time-lapse seismic response in heavy oil reservoirs, one must consider a more detailed analysis than typical amplitude difference or time-shift approaches. With the varied fluid, pressure and temperature changes associated with EOR techniques, a binary, qualitative approach to interpretation is insufficient to properly characterize the changes in the reservoir. For this study, only fluid influences were considered and included in the 4D rock physics inversion, but if pressure and temperature data were available, the rock physics modeling and inversion could be extended to include pressure and temperature influences. In the absence of this data, a first order approximation is made to calculate the pore pressure in the reservoir using the acoustic velocity change derived from the time shift volume. The resulting steam saturation, oil saturation and pore pressure volumes demonstrate the significant reservoir heterogeneity and together can lead to more economically and environmentally sustainable oil production by identifying baffles/barriers, inefficient steam zones, escaped oil and escaped steam and zones of either over-pressure or pressure depletion.

Barker et al. (2016) performed a study in a CSS environment in the Peace River with access to over 700 seismic vintages. They used a combination of amplitude changes and time-shifts to observe the combination of multiple production related effects (i.e. pressure, temperature and saturation). This work highlights the complex coupling of saturation changes with pressure and temperature changes. Justyna et al. (2015) elaborate further on the difficulty of disentangling between these phenomena using only time-shift analysis as velocity decreases are indicative of either pressure increases, temperature increases or gas saturation increases and separating these responses without prior knowledge from observation wells is often not feasible. If one considers a section plot of the inverted acoustic impedance change from Figure 6-1, one could make an interpretation that the observed hardening (increases in AI) surrounding the softening (steam) events could in fact be real pressure hardening related to gas saturation decreases caused by pressure “pushing” gas back into solution as noted in the studies by Justyna et al. (2105) and Barker et al. (2016), but two important differences led to the interpretation that this is side-lobe energy. First, I note that in the Justyna et al. and Barker et al. studies, monitoring of the reservoir began after production related depletion had taken place, wherein the production had decreased reservoir pressure to the extent that gas was beginning to come out of solution. Subsequently, when monitoring began and steaming recommenced, pressure increased and gas went back into solution. In this study, the baseline survey was acquired with virgin reservoir conditions, thus this phenomena would not be expected. Second, in the aforementioned studies, the amplitude increase or hardening that was observed was corroborated by an associated decrease in travel time observed in the time-shifts between surveys. This travel time decrease was not observed in this study and as such, the increases in AI observed in the final inversion results are interpreted as side-lobe energy. This example demonstrates that even after careful conditioning and modeling, there are limitations to the quantitative results that must be considered in the interpretation.

As a final note, it should be mentioned that perhaps one of the most important conclusions from this study is that a proper study design from the outset of a project will lead to a more robust and accurate final result with less uncertainty and less assumptions during interpretation. In particular, although not mentioned in detail in this thesis, a great deal of time and effort was spent in pre-conditioning the seismic data in preparation for inversion. Acquisition with the exact same parameters could greatly improve survey repeatability and therefore decrease the amount of pre-conditioning needed. Additionally, although the seismic data were processed in a 4D friendly manner with subsequent AVO inversion in mind, a more collaborative approach between the processing and the interpreter/AVO analysis would lead to a better understanding of data limitations and data quality. In this case, the processing was completed prior to the commencement of this study, therefore the processing flow applied is assumed to be optimum, but this is not known. For rock physics modeling, laboratory measurements of elastic properties at various pressure and temperature states with varying rock composition and pore fills would allow the generation of a rock physics model that explicitly accounts for and separates between fluid effects and geomechanical effects thereby de-coupling these parameters and resulting in a much more realistic interpretation of the 4D AVO anomalies. Finally, in an ideal case, any 4D project should have access to time-lapse calibration data to validate the inversion results. This could take the form of production, injection, pressure or temperature data, or elastic log data from observation wells. If all these data and planning were to take place before the outset of any similar subsequent study, I believe the results would improve significantly. As it stands, although the methodology applied in this study is considered robust, the final quantitative 4D rock physics inversion results contain a high degree of uncertainty and a proper interpretation requires care and acknowledgement of this fact.

References

Aki, K., and Richards, P.G., 1980, Quantitative Seismology. W.H. Freeman & Co.

Bachrach, R., and Avseth, P., 2008, Rock physics modeling of unconsolidated sands: Accounting for non-uniform contacts and heterogeneous stress fields in the effective media approximation with applications to hydrocarbon exploration: Geophysics, 73, no. 6, 197-209.

Barker, T., Xue, Y., 2016, Inversion of continuous 4D seismic attributes to reveal daily reservoir changes: SEG Annual Meeting Technical Program Expanded Abstracts.

Batzle, M., and Wang, Z., 1992, Seismic properties of pore fluids: Geophysics, 57, 1396-1408.

Blackman, R.B., and Tukey, J.W., 1958, The measurement of power spectra from the point of view of communication engineering: Dover Publications, 190.

Cho, D., Coulombe, C., and Margrave, G., 2011, On the extraction of angle dependent wavelets from synthetic shear wave sonic logs: CREWES Research Reports, 2011.

Chopra, S., Lines, L., Schmitt, D., and Batzle, M., 2010, Heavy Oils: Reservoir Characterization and Production Monitoring. SEG Geophysical Developments, 13.

Conoco-Philips AER Annual Performance Presentation (2015). Subsection 3.1.1 (2f), p.30.., https://www.aer.ca/documents/oilsands/insitu-presentations/2015AthabascaConocoSurmontSAGD94609426.pdf

Domenico, S.N., 1976, Effect of brine-gas mixture on velocity in an unconsolidated sand reservoir: Geophysics, 41, 882-894.

Dix, C.H., 1955, Seismic velocities from surface measurements: Geophysics, 20, 68=86.

Gardner, G.H.F, Gardner L.W, and Gregory, A.R., 1974, Formation velocity and density – the diagnostic basics for stratigraphic traps: Geophysics, 39, 770-780.

Gassmann, F., 1951, Elastic wave through a packing of spheres: Geophysics, 16, 673-685.

Gray, D., Day, S., and Schapper, S., 2015, Rock Physics Driven Seismic Data Processing for the Athabasca Oil Sands, Northeastern Alberta, CSEG Recorder, 40, 32-40.

Gray, D., Wagner, K., and Naidu, D., 2016, 3C-4D locates mobile bitumen in oil sands reservoirs: GeoConvention 2016 Expanded Abstracts.

Gray, D., Todorovic-Marinic, D., Larson, G., Zhang, J., Naidu, D., Letizia, M., Wagner, K., and Palka, M., 2018, Forecasting bitumen state and production from 3C-4D seismic: CSEG luncheon abstract, January 24th, 2018.

Greenberg, M. L., and Castagna, J. P., 1992, Shear-wave velocity estimation in porous rocks; theoretical formulation, preliminary verification and applications: Geophysics Prospecting, 40, 195-209.

Hein, F.J., Landenberg, C.W., Kidston, C., Berhane, H., and Berezniuk, T., 2001, A Comprehensive Field Guide for Facies Characterization of the Athabasca Oil Sands, Northeast Alberta: Alberta Energy and Utilities Board, Alberta Geological Survey.

Japex 2017, Start of Production Operations in Oil Sand Project at Hangingstone in the Province of Alberta, Canada, and Decision not to Re-start SAGD Operations in the 3/75 Section Area. http://www.japex.co.jp/english/newsrelease/pdfdocs/JAPEX20170808_Hangingstone_HEcommence_DEMOnotrestart_e.pdf

Kato, A., Onozuka, S., and Nakayama, T., 2008, Elastic property changes in a bitumen reservoir during steam injection: The Leading Edge, 1124-1131.

Kelly, B., 2012, Processing and interpretation of time-lapse seismic data from a heavy oil field: Ph.D. Thesis, University of Calgary.

Kelly, B., and Lawton, D., 2013, Interpretation of Time-Lapse Seismic Data from a Heavy Oil Field, Alberta, Canada: CSEG Recorder, 38, 27-40.

Kelly, B., Cho, D., and Rowell, C., 2015, The Nexen Time-lapse Project: An Industry Leading Approach to Reservoir Monitoring and Recovery: SEG Annual Meeting Technical Program Expanded Abstracts.

Lines, L. R., Daley, P.F., and Ibna-Hamid, L., 2010, The accuracy of dipole sonic logs and its implications for seismic interpretation: Journal of Seismic Exploration, 19, 87-102.

Mesdag, P., Saberi, M., and Mangat, C., 2015, Updating the low-frequency model in time-lapse seismic inversion: A case study from a heavy-oil steam-injection project, The Leading Edge, 1456-1461.

Milovac, J., 2009, Rock physics modeling of an unconsolidated sand reservoir: Master's Thesis, University of Houston.

Mindlin, R. D., 1949, Compliance of bodies in contact: Journal of Applied Mechanics, 16, 259-268.

Nakayama, T.,Takahashi, A., Skinner, L., and Kato, A., 2008, Monitoring an oil-sands reservoir in northwest Alberta using time-lapse 3D seismic and 3D P-SV converted wave data: The Leading Edge, 1158-1175.

Nasser, M., Maguire, D., Hansen, H. J., and Schiott, C., 2016, Prestack 3D and 4D seismic inversion for reservoir static and dynamic properties: The Leading Edge, 415-422

Przybsyz-Jarnut, J.K., Dldraga, C., Potters, J.H.H.M, Lopez, J.L., La Follet, J.R., Willis, P.B., Bakku, S.K., Xue, Y., and Barker, T.B., 2015, Value of Information of Frequent Time-Lapse Seismic for Thermal EOR Monitoring at Peace River: SPE Annual Technical Conference, SPE-175046-MS.

Rider, M., and Kennedy, M., 2011, The Geological Interpretation of Well Logs. 3rd Edition. Rider-French Consulting Ltd., Glasgow, Scotland.

Walton, K., 1987, The effective moduli of a random packing of spheres: Journal of the Mechanics and Physics of Solids, 33, 213-226.

Westang, K., Hansen, H., Rasmussen, K., 2009, ISIS Rock Physics – A new petro-elastic model for optimal rock physics inversion with examples from the Nini Field: Sound of Geology Workshop 2009.

Yilmaz, O., 2001, Seismic Data Analysis: Processing, Inversion and Interpretation of Seismic data: Investigations in Geophysics, 10.

Zeigler, L.M., 2013, Modeling and mapping the effects of heat and pressure outside a SAGD chamber using time-lapse multicomponent seismic data, Athabasca oil sand, Alberta: Master's thesis, Colorado School of Mines.

Zhang, J., and Larson, G., 2016, Monitoring steam chamber movement using time-lapse PP-PS joint inversion: SEG Annual Meeting Technical Program Expanded Abstracts, 2956-2960.